Journal of Hazardous Materials 489 (2025) 137546

Contents lists available at ScienceDirect

Journal of Hazardous Materials

journal homepage: www.elsevier.com/locate/jhazmat

Fibrous erionite modifications following THP-1 macrophage phagocytosis: An insight into the mechanisms of interaction with biological systems

Paolo Ballirano [a,b,*], Alessandro Pacella [a], Serena Mirata [c,d], Mario Passalacqua [d,e], Maria Cristina Di Carlo [a], Lorenzo Arrizza [a], Maria Rita Montereali [f], Sonia Scarfì [c,d]

[a] Department of Earth Sciences, Sapienza University of Rome, Piazzale Aldo Moro 5, Rome I-00185, Italy
[b] Rectorial Laboratory Fibres and Inorganic Particulate, Sapienza University of Rome, Piazzale Aldo Moro 5, Rome I-00185, Italy
[c] Department of Earth, Environment and Life Sciences, University of Genova, Corso Europa 26, Genova I-16132, Italy
[d] Inter-University Center for the Promotion of the 3Rs Principles in Teaching & Research (Centro 3R), Pisa I-56122, Italy
[e] Department of Experimental Medicine, University of Genova, Viale Benedetto XV 1, Genova I-16132, Italy
[f] Italian National Agency for New Technologies, ENEA, Casaccia Research Centre, Via Anguillarese 301, S. Maria di Galeria, Rome I-00123, Italy

HIGHLIGHTS

- Upon macrophage phagocytosis, erionite releases significant cations.
- Release is counterbalanced by hydronium ions sequestration from lysosomes.
- Sequestration provokes quick pH dysregulation.
- Restoration by hyperactivation of ATP-dependent proton pumps causes mitochondrial suffering.
- This suffering leads to chronic inflammation and possibly cancer development.

GRAPHICAL ABSTRACT

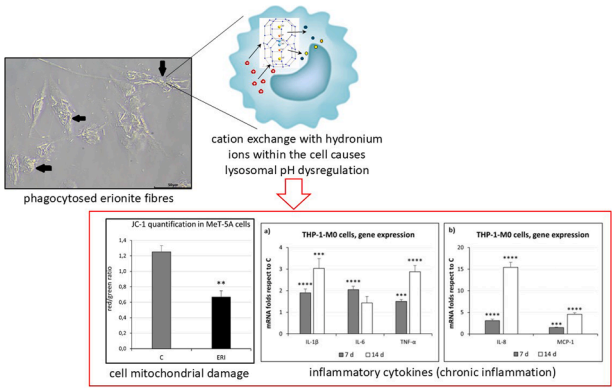

ARTICLE INFO

Keywords:
Erionite
THP-1 macrophages
Phagocytosis
Mitochondrial damage

ABSTRACT

Erionite is a ubiquitous natural zeolite, often occurring with fibrous habit, whose strong tumorigenic activity to humans has been certified by its inclusion in the Group 1 Human-Carcinogenic list by the International Agency for Research on Cancer. To date, the reason(s) of erionite toxicity are still unclear, albeit several hypotheses have been proposed. The present work, based on the combined analysis of the chemical and structural modifications of erionite fibres following incubation in human THP-1 macrophages and evaluation of cellular response, indicates that, upon macrophage phagocytosis, a large release of cations is counterbalanced by a significant sequestration of hydronium ions from lysosomes provoking a quick pH dysregulation. This would be restored by the hyperactivation of ATP-dependent proton pumps with significant energy expenditure for the cell, ultimately causing mitochondrial suffering, leading to chronic inflammation and eventually cancer development.

* Corresponding author at:Department of Earth Sciences, Sapienza University of Rome, Piazzale Aldo Moro 5, Rome I-00185, Italy.
E-mail address: paolo.ballirano@uniroma1.it (P. Ballirano).

https://doi.org/10.1016/j.jhazmat.2025.137546
Received 4 October 2024; Received in revised form 17 January 2025; Accepted 7 February 2025
Available online 10 February 2025

1. Introduction

Erionite (ERI) is an "intermediate" zeolite (Si/Al range 2.13–3.76, mean 3) that belongs to the small pore family, being characterized by the presence of eight-ring pores in its structure (largest opening 3.6 ×5.1 Å) [1,2]. It crystallizes in the hexagonal crystal system, space group $P6_3/mmc$ and has an average formula $K_2(Na,Ca_{0.5})_8[Al_{10}Si_{26}O_{72}] \bullet 30\ H_2O$ [3,4]. Because of its large chemical variability three different species, erionite-K, -Na, and -Ca, are recognized depending on the most abundant extra framework (EF) cation [4–7]. Moreover, erionite is a member of the ABC-6 family i.e. it is built from the stacking along the *c*-axis, following an ABC scheme, of layers made of hexagonal rings of TO_4 (T = Si,Al) tetrahedra [8]. Erionite is characterized by a six-layer period following the sequence AABAAC. In theory, 10 different sequences for a period of six-layers are possible [9,10], but only four of them occur in nature: AABAAC erionite, AABBCC chabazite [11], ABBACC bellbergite [12], ABABAC liottite [13]. The framework of erionite consists of columns of alternating cancrinite (ε) cages, and double 6-rings (d6r) plus erionite cages (23-hedra) that are generated by linking adjacent columns via single 6-rings (s6r) at the level of ε-cages [14,15]. The unit cell hosts two cancrinite cages and two d6r alternating along 0, 0, *z*, and two erionite cages running, respectively, along 1/3, 2/3, *z*, and 2/3, 1/3, *z*. Cages host EF cations and H_2O and, in particular, the small ε cage allocate a K^+ ion at its centre (site labelled as K1) whereas the large erionite cage potentially contains several cation sites prevalently residing at or near the axis of the cage of which those labelled Ca1, Ca2 and Ca3 are consistently found [7,16–18]. Moreover, K-rich erionite samples (> 2 K^+ atoms per formula unit a.p.f.u.) display a further EF cation site, labelled K2, which is placed at the centre of the boat-shaped eight-ring forming the walls of the erionite cage [7,19–21]. The population of the EF cations sites is influenced by short contacts imposing mutual exclusions. H_2O is distributed among six OW sites (OW7–12) radiating from the axis of the cavity and placed at special positions *x*, 2*x*, *z* (or ¾), whose distribution, as in the case of EF cations, is dictated by prevention of short contacts.

Recent substantial work has been devoted to analysing in detail the cation exchange properties of erionite fibres finalized to building a solid background for modelling their interaction with biological environments. The relevant interest of this topic is related to the unambiguous link of inhalation by humans of erionite fibres with the onset of malignant mesothelioma (MM). In fact, *in vivo* studies have proved the strong tumorigenic activity of erionite [22] that has been accordingly included in the Group 1 Human-Carcinogenic list by the International Agency for Research on Cancer (IARC) [23,24]. Erionite occurs worldwide and, in particular, a high rate of MM observed in several villages of Central Anatolia have been related to inhalation of erionite fibres since the 1970s [25]. The outstanding potential of erionite in causing malignant mesothelioma is ascertained [26,27]. Its mesothelioma- and tumour-inducing potential in rats and other animals has been reported to be several hundreds of times greater than that of "asbestos" [28–31]. It has been proposed that erionite fibres induce necrotic cell death leading to release of high-mobility group protein 1 (HMGB-1) in the extracellular space [32]. The release causes a chronic inflammatory response, macrophage recruitment and the secretion of TNF-α which in turn activates NF-κB, leading to the overall survival of mesothelial cells that have accumulated genetic damage due to exposure to the mineral fibres. Gualtieri has recently [33] listed several factors potentially playing a relevant role in the toxicity/carcinogenicity potential of erionite. The most relevant being:

1) biodurability, that is exceptionally high in erionite and exceeds that of amphibole asbestos fibers;
2) cation exchange. Erionite can exchange its extra framework cations K^+, Na^+, Ca^{2+}, and Mg^{2+} in both intracellular and extracellular environments, eventually disrupting the intracellular homeostasis and leading to cell death. In addition, exchange of Ca^{2+} may potentially interfere with the intracellular calcium crosstalk regulating cell functions and apoptosis [33];
3) the role of iron, that occurs under the form of iron-rich impurities located at the surface of the fibres [34]. The impurities can dissolve during acidic macrophage phagocytosis contributing to the production of reactive oxygen species (ROS). Moreover, because of the ion-exchange capabilities of erionite, fibres can accumulate iron on their surface and/or at specific sites at the opening windows of the zeolite channels [35–37], and this iron may participate in oxidative reactions damaging the DNA [35,38];
4) exchangeable trace toxic metals as As, Be, Al and Pb can be released by cation exchange both in intracellular and extracellular environments contributing to ROS production [39];
5) Besides these chemical-physical parameters reported in 1)-4), genetic susceptibility is also invoked to explain the high potency of erionite in inducing malignant mesothelioma in humans. Carbone and coworkers [27] have postulated a model to explain the erionite-induced mesothelioma morbidity in the population of some Cappadocian villages (Karain, Sarihidir, and Tuzkoy) based on the genetic susceptibility by inheriting mutations of the onco-suppressor *BAP1* gene. Reduced levels of *BAP1* in heterozygous $BAP1^{+/-}$ individuals are responsible for the reduction of both IP3R3 levels and calcium flux, preventing $BAP1^{+/-}$ cells that accumulate DNA damage from executing apoptosis, and determining a higher probability of proliferation of aberrant cells which may ultimately result in the onset of cancer [40].

Starting from the pioneering paper by Ballirano and Cametti [41] where fibres were incubated in artificial lysosomal fluid (ALF) and Gamble's solution, following the complications to control the stability of these simulated lung fluids (SLFs) over a large span of time, many papers adopted simplified formulations [42,43] or focused on the ability of erionite to upload specific cations [36,37,44,45]. Simulated formulations lack most of the organic components and, in the case of the simplified ones, even some minor inorganic salts are substituted to avoid possible interference with the released cations during analytical procedures. However, it is unclear whether those simplifications represent a sufficiently close approximation of the conditions to which fibres are subjected in the biological compartment after inhalation and inside the cells after phagocytosis performed by activated alveolar macrophages. These cells are the first line of defence by the immune system in the lung and the first cells to actively internalise foreign particles with the aim to efficiently clean up the alveolar space averting infections and/or the deposition of hazardous foreign bodies in the lung parenchyma. Thus, *in vivo* all mineral fibres/particles with a length/size $\leq$ 15 μm sooner or later are phagocytosed by macrophages [46]. In the case of erionite this may very likely cause the alteration of both the fibre surface as well as of the intracellular environment and homeostasis by releasing and recharging its cationic cargo through interaction with the surrounding milieu. In a recent work, it has been described for the first time, by synchrotron micro-X-ray fluorescence, the spatial distribution of metals and other cations in macrophage cells after the phagocytosis of erionite fibres up to four days of incubation [47]. The results of this research ruled out the intracellular Ca^{2+} binding by the fibres, in exchange with Na^+, as one of the mechanisms of toxicity of erionite fibres, a hypothesis that has been proposed, among others, to explain erionite hazard potential [33]. Thus, the molecular mechanisms by which the erionite cation exchange properties unravel their damage potential inside the cells still lack an exhaustive explanation. Furthermore, these processes can also occur in mesothelial cells due to their phagocytic capacity, likely concurring to the alteration of the intracellular biochemical homeostasis and contributing to the final onset of cancer. To shed further light into these complex mechanisms, in this work we describe, by a multi analytical approach, the structural modifications and the cellular biochemical alterations induced by the *in vitro* phagocytosis of erionite fibres by THP-1 cell line derived macrophages mimicking the action of

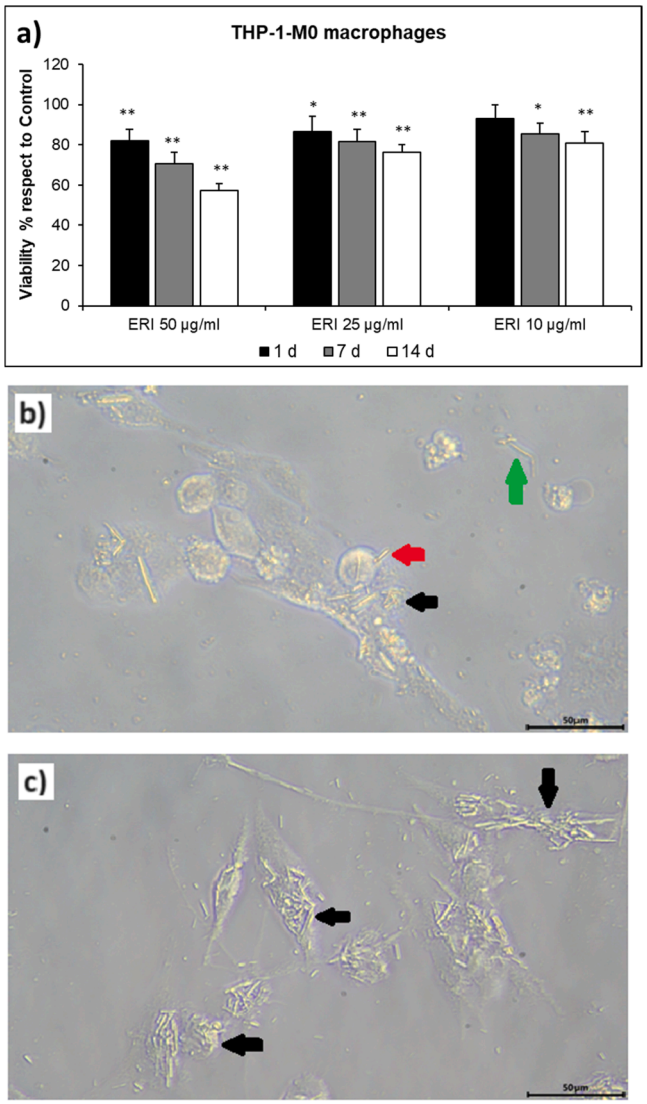

Fig. 1. Erionite fibre toxicity and phagocytosis by THP-1 macrophages. a) MTT assay on THP-1 macrophages incubated with different fibre concentrations for 1, 7 and 14 d. Asterisks indicate significance in paired Tukey test (ANOVA $p < 0.00005$; Tukey vs. C, $*p < 0.05$; $**p < 0.01$). b) and c) White-field representative micrographs of THP-1 macrophages incubated for 1 d or 7/14 d with erionite fibres, respectively. Black arrows indicate phagocytosed fibres; red arrow a fibre in the process of being phagocytosed; green arrow a non-phagocytosed fibre deposited on the plate surface. The black bars span 50 µm.

the cellular first line of defence in the alveolar space against inhaled harmful stimuli [48]. The macrophage model was chosen as the best representative of cells with phagocytic capacity for its optimal scavenging properties allowing the subsequent retrieval of a suitable number of phagocytosed fibres for the chemical-physical characterization studies. Moreover, we report the results of a thorough chemical structural investigation aimed at identifying possible experimental interferences induced by manipulation during experiments that, coupled with the careful check of control samples, will shed new perspectives toward the comprehension of the mechanism(s) inducing toxicity of erionite in comparison to simplified models.

2. Methods

2.1. Sample description and incubation in THP-1 macrophages

Fibres of erionite from Rome (Oregon, USA) were chosen for the following experiments. The raw material was enriched in erionite content (up to ca. 95 wt%) according to the procedure reported in reference 26. Fibre length and diameter were in the range of ca. 5–70 µm and 0.1–3.0 µm, respectively, with most fibres (65 %) showing length below 20 µm and width less than 5 µm. For experiments in THP-1-derived macrophages, sterile fibre suspensions were prepared [49,50]. Fibres were administered to THP-1 macrophages without any pre-treatment into fluids mimicking their passage through the respiratory system. However, the neutral pH of the fluids as well as the Na^+, Ca^{2+}, K^+, and $Mg2^+$ ion concentrations of the respiratory fluids are reproduced also in the cell medium in which the fibres are immersed before the phagocytosis occurs, *de facto* mimicking the extracellular body fluids. This, added to the relatively short amount of time requested for the fibre deposition into the alveolar space makes the possible modifications prior phagocytosis quite negligible compared to those observed in the acidic environment of the lysosomes.

The human monocytic cell line THP-1 was obtained from the American Type Culture Collection (LGC Standards srl, Milan, Italy) and cultured at 37 °C in a humidified 5 % CO_2 atmosphere. THP-1 cells were cultured in RPMI-1640 with L-glutamine (Euroclone, Milan, Italy) and 10 % FBS (Euroclone).

Erionite toxicity was initially evaluated by the MTT assay to assess the degree of cell damage given by the erionite working concentration used in the following experiments. In brief, THP-1 cells were seeded at 50,000 cells/well in 96-well plates and then polarised into M0 macrophages by adding 30 ng/mL phorbol-12-myristate 13-acetate (PMA, PeproTech EC, London, UK) to the culture medium for 24 h [50]. Polarization to the M0 phenotype was assessed by gene expression quantification of CD163, CXCL10 and mannose receptor (MRC1) differentiation markers by qPCR as shown in Fig. S1. Differentiated macrophages were then exposed to 10, 25, 50 µg/mL of erionite for 1 d, 7 d, and 14 d, changing half of the cell medium in the wells every three days, in the longer incubation times. At the end of the different incubation times, the MTT assay was performed as described in reference 51. The linearity of MTT absorbance in the cell range used in the experiments was assessed by performing the MTT on a standard curve obtained with serial dilutions of THP-1 M0 cells in the 6250–50,000 cells/well range. The derived linear regression graph is reported in the Supplementary material (Fig. S2) showing the trend line equation and the R2 data correlation. The MTT cytotoxicity test on erionite-exposed cells showed that, at the highest concentration tested, 50 µg/mL, the mortality rate of macrophages was around 20 % after 1 d and reached a maximum of 40 % after 14 d of incubation (Fig. 1a). Thus, since more than 50 % of the cells were still alive in the culture, even after 14 d of exposure, this concentration was chosen for the phagocytosis experiments because it could ensure a significant fibre uptake from macrophages avoiding excessive cell damage that would compromise the retrieval of *bona fide* internalised fibres.

To obtain the phagocytosed erionite fibres, THP-1 cells were seeded at 3×10^6 cells/plate in 10-cm plates and differentiated to M0 macrophages by adding 30 ng/mL PMA to the culture medium for 24 h [51]. Then, M0 macrophages were treated with 50 µg/mL of erionite for 1 d, 7 d, and 14 d (THP-1–1d, −7d, −14d). For the 7 d and 14 d experiments cell media were changed every three days. After the incubation period, cells were washed twice with PBS before 15 mL of lysis solution (10 % HPLC grade methanol in sterile milli-Q® Ultrapure water) were added to the remaining THP-1 cells in the plates, to ensure that only phagocytosed fibres were retrieved through this procedure. After thoroughly mixing, the cell lysate containing the fibres was centrifuged at 4000 rpm for 10 min. The pelleted fibres were washed twice more using 15 mL of lysis solution, to remove the cellular debris. Then, the fibres were resuspended in 1 mL of lysis solution and centrifuged at 10,000 rpm for 10 min. After this washing step was repeated three times, erionite fibres were left to dry overnight under a laminar flow hood. Additionally, a control containing only pristine erionite fibres was prepared as well. Indeed, a comparable amount of fibrous erionite was suspended and

washed in lysis solution as described above before erionite fibres were dried under a laminar flow hood. Experiments were carried out in duplicate. In the second set of experiments all step were identical to what previously described, differing exclusively for a more prolonged washing procedure of the fibres once retrieved from inside the cells (fibres washed 3 more times in lysis buffer prior drying under the laminar hood flow).

By using the above-mentioned concentration, a significant number of erionite fibres were found inside macrophages already after 1 d of incubation and all fibres in the petri dishes were internalised after 7/14 d of exposure as displayed in the micrographs of Fig. 1b-c.

The quantity of recovered fibres phagocytosed by THP-1 cells was of the order of a few hundred μgrams for each experiment. The relatively large number of recovered fibres assures that they represent an average picture of the phagocytosis process where a fibre is internalized in an endocytic vesicle that, subsequently, evolves via different models (maturation, vesicular, kiss-and-run, hybrid) to lysosome [52]. During the whole process, fibres may enter in contact with different chemical-physical environments since pH ranges from 4.5 to 5 within the lysosome (luminal environment maintained at the proper pH by proton pumping vacuolar ATPases) to 7.4 within the cytosol. Apart from the main experiments, additional ones were performed to investigate the possible occurrence of interferential effects during the manipulation of fibres pre- and post-incubation and to provide additional hints on the effect of single physical-chemical parameters. The additional samples were:

A) Control samples prepared by incubation of the fibres for 1 d into the same media used for cell culture:
   a. Phosphate Buffered Saline (PBS) (*control PBS*);
   b. Roswell Park Memorial Institute (RPMI) medium (*control RPMI*).
B) Suspension of fibres for 1 h in distilled water kept at a pH 4.5 by proper addition of HCl (*H_2O pH 4.5*).
C) Suspension of fibres in ALF for 14 d (*ALF 14d*). ALF is analogous to the fluid with which inhaled particles would come into contact after phagocytosis by alveolar and interstitial macrophages in the lung [53].
D) Post-immersion for 1 d of fibres retrieved inside THP-1-derived macrophages after 7 d phagocytosis in the following buffers:
   a. PBS (*THP-1 PBS*);
   b. RPMI (*THP-1 RPMI*).

The fibres were then recovered using the same procedure illustrated above.

2.2. SEM-EDS

The chemical composition of the pristine fibres and those after immersion in ALF was determined using a Quanta 400 SEM equipped with an EDS Genesis system (FEI, Hillsboro, OR, USA). Analytical conditions were: 15 kV accelerating voltage, 11 mm working distance, 0° tilt angle. The crystal chemical formulae were calculated based on 36 (Si+Al) atoms per unit formula (a.p.f.u.), assuming a water content of 18.5 wt% (corresponding to ca. 30 H_2O p.f.u.). Both the balance error formula E% and the K content test (K content $\geq$ 2 a.p.f.u.) were used for selecting the positive analyses (Table S6) [54]. The analysis of the fibres after phagocytosis from THP-1-derived macrophages revealed E% values markedly outside the admitted range of $\pm$ 10 % (up to 40 %), so that it was not possible to obtain reliable crystal chemical formulae, likely due to both possible occurrence of a layer of organic material with variable thickness on the fibre surface and fibre alteration following the phagocytosis process. Nonetheless, in this case a qualitative interpretation of the spectra (Fig. S4) is given.

2.3. Powder X-ray diffraction (PXRD)

PXRD data were collected using a Bruker AXS D8 Advance operating in transmission mode, θ/θ geometry. The instrument is fitted with focusing (Göbel) mirrors and a position sensitive detector (PSD) VÅntec-1 placed after radial Soller slits. Samples were loaded into the tip of 0.3 mm diameter borosilicate glass capillaries sealed at both ends. The length of the powdered sample was in the 6–8 mm range and for this reason it was carefully placed at the centre of the beam whose sagittal length is of 12 mm. Patterns were measured in the 6–145 °2θ angular range, 0.0218 °2θ step-size and 20 s counting time using CuKα radiation. The pristine (PRI) sample contains minor chabazite and quartz plus clay minerals (identified as nontronite, an iron-rich phyllosilicate) [34,43]. Preliminary analysis of the diffraction data pointed out the significant reduction of the clays content upon incubation/internalization. Data were evaluated by performing a mixed Pawley-Rietveld method, successfully adopted for similar samples [42–44], using Topas V6 and the Fundamental Parameters Approach [55,56]. However, to assure a consistent modelling of the clay phase, the Pawley contribution was limited to the main three reflections (occurring at a position $> 6°$ 2θ) reported in the PDF 29–1497 of nontronite (100, ca. 19.6°; 111, ca. 34.8°; 118, ca. 61.5°) whose positions were constrained to a trigonal/hexagonal cell having a = ca. 5.2 Å, c = ca. 14.75 Å. The intensity proportion among the three reflections, as refined in the PRI sample where they are clearly apparent, was kept constant in all refinements. This is crucial as the three peaks occur under the tails of reflections of erionite and in the absence of constraints, in the presence of small amounts of clay, the refined intensity may vary in uncontrolled way impacting important parameters of the erionite structure as it was observed in preliminary unconstrained refinements. Both sets of samples were characterized by the occurrence of erionite, chabazite, and traces of quartz. However, the first set had a slightly greater content of clays that was reasonably removed by the prolonged washing of fibres applied during the preparation of the second set of samples. Moreover, in the case of THP-1–1d, we observed the occurrence of a small, isolated peak that was attributed to the strong 104 reflection of calcite. This reflection was approximated by a single peak, not related to any structure, whose position, width, and intensity were refined as a part of the fitting. It is interesting to notice that in the same sample of the first set we observed the precipitation of a more abundant quantity of calcite as well as traces of apatite that was not found in the sample of the second set (Fig. S3). Starting structural data of the various phases were as follow: erionite-Na [43], chabazite [57], and quartz [58]. Fractional coordinates and site occupancies of both EF cations and H_2O sites were refined for erionite. Cell parameters were refined for both erionite and chabazite. The attempt to displace the Ca2 site from special position 1/3, 2/3, z to x, $2x$, z (i.e. not perfectly aligned along the axis of the erionite cavity), to reach a more favourable coordination to oxygen atoms, failed producing unstable refinements and a very marginal improvement of the statistical indicators. For this reason, final refinements were performed with Ca2 at 1/3, 2/3, z. Several models of anisotropic broadening were checked to describe the peak shape of erionite to keep into account its fibrous morphology [59]. The best performing one was by means of normalized symmetrized spherical harmonics function [60], implemented into the command *spherical_harmonics_hkl* of Topas V6, acting on the Lorentzian half-width of the reflections. Absorption correction was performed considering a cylindrical sample [61] and the correlation between displacement parameters and absorption was handled according to [62]. Normalized symmetrized spherical harmonics were also used to cope with preferred orientation effects by selecting the number of appropriate terms (8th-order, six refinable parameters) according to [63]. Individual parameters were very close to zero, coherently with the preparation of the samples as capillaries. Refined structural parameters of erionite included fractional coordinates and site occupancy fraction (s.o.f.) of EF cations and H_2O sites. Isotropic displacement parameters were refined and constrained as follow: $B_{T1} = B_{T2}$; $B_{O1} = B_{O2} = B_{O3} = B_{O4} = B_{O5}$

$= B_{O6}$; $B_{K1} = B_{K2}$; $B_{Ca1} = B_{Ca2} = B_{Ca3} = B_{Ow8} = B_{Ow9} = B_{Ow10} = B_{Ow11} = B_{Ow12} = 2\ ^*B_{Ow7}$ to minimize correlations. The results of the refinements from the two data sets are almost overlapping and for this reason we will report exclusively those arising from the second group of samples. CIF files of the various samples are available for download at the journal site. Miscellaneous data of the refinements, including statistical indicators, and cell parameters of erionite samples are reported in Table S2, refined site scattering (s.s. in e^-) at individual EF cation and H_2O sites are listed in Table S3, fractional coordinates of EF cation and H_2O sites are reported in Table S4, and refined T-O bond distances in Table S5. A representative example of final Rietveld plots (sample THP-1–14d) is shown in Fig. S5.

2.4. Incubation of the fibres in artificial lysosomal fluid (ALF)

Dissolution experiments were carried out in ALF based on the formulation reported in reference 53. An amount of 20 mg of sample was placed in a Falcon™ polypropylene tube, suspended and then stirred in 40 mL of solution. The tubes were fully immersed in a thermostatic water-bath and held at a constant temperature of 37 ± 1 °C for the entire duration of the dissolution tests. A blank procedure was always performed for each set of experiments. Samples were incubated up to 15 days.

At the end of the experiment the solution was sampled from the tube with a syringe and filtered using a nitrocellulose membrane filter with a 0.22 μm pore size. Fibres were recovered on filters and rinsed with ultrapure deionized water for excluding residues of the solution.

2.5. Inductively coupled plasma optical emission spectroscopy (ICP-OES) investigation

ICP-OES was employed to measure the concentration of leached extra-framework cations Mg, Ca, and K from the erionite fibres both in ALF and water at pH of 4.5. It must be pointed out that, for ALF experiments it was not possible to measure the Na release due to its high content in the solution. One cm^3 of each filtered solution was diluted (1:20) with a 1 % nitric acid solution and analysed. All measurements were performed using a Perkin–Elmer Optima 2000 DV ICP-OES spectrometer (Perkin-Elmer, USA) equipped with a cross flow nebulizer placed inside a Scott spray chamber. ICP Aristar (BDH) standard solutions in nitric acid for Mg, Ca, and K were used to make up the calibrating solutions for ICP-OES analyses. To ensure adequate quality assurance, the measures of the standard solutions were regularly repeated after the measurements of each single experiment. Data are the average values of duplicate measurements (corrected for the blank).

2.6. Confocal microscopy analyses

THP-1 cells were seeded at 75,000 cells/well in eight-well Lab-Teck chambered slides (Nalge Nunc Int., Naperville, IL, USA) and, once differentiated, M0 macrophages were treated with erionite fibres (50 μg/mL) for 6 h, 24 h, or 72 h. MeT-5A cells were plated at 5000 cells/well in eight-well Lab-Teck chambered slides and, the following day, cells were treated with 50 μg/mL of erionite fibres for 72 h. After cells were stained with the different fluorescent dyes following the manufacturer's instructions, images were immediately acquired in fluorescence mode using a Nikon AX R confocal microscope equipped with a PLAN APO 60x oil objective (NA 1.42) (Nikon Europe, B.V., Amstelveen, The Netherlands).

To measure the mitochondrial damage induced by erionite fibres, cells were stained with the mitochondrial proton gradient (ΔΨ)-sensitive fluorescent dye JC-1 (Thermo Fisher Scientific, Waltham, MA, USA) which exhibits potential-dependent accumulation in mitochondria. At low membrane potentials, JC-1 exists as a monomer and produces a green fluorescence (emission at 527 nm), whereas, at high membrane potentials, JC-1 forms aggregates and produces a red fluorescence (emission at 590 nm). Thus, mitochondrial depolarization is indicated by a decrease in the red/green fluorescence intensity ratio [64]. Images were obtained acquiring the green fluorescence (emission at 527 nm) and the red fluorescence (emission at 590 nm). Then, the red/green fluorescence intensity of selected ROIs in each image (at least five microphotographs taken for each condition) was quantified after background subtraction with the ImageJ software (v1.8.0, National Institutes of Health, Bethesda, MD, USA), and the results were expressed as the mean red/green ratio ± SD of the different samples compared to control, untreated cells.

To assess the lysosomal pH following exposure to erionite, live cells were marked with the fluorescent pH indicator LysoSensor™ Green DND-189 (pK_a 5.2), which accumulates in acidic organelles and exhibits a pH-dependent increase in fluorescence intensity upon acidification. Moreover, to investigate whether the lysosomal pH dysregulation was correlated with the hyperactivation of ATP-dependent proton pumps, cells were pre-treated with 50 nM Bafilomycin A1 (a specific inhibitor of vacuolar H^+-ATP-dependent pump) for 30 min before exposure to erionite fibres for 6 or 24 h. Images were obtained acquiring the green fluorescence (emission at 505 nm). Then, the green fluorescence intensity of each image (at least three microphotographs taken for each condition) was quantified after background subtraction with the ImageJ software and then normalised on the cell number. Since lysosomal pH increase is indicated by a decrease in the green fluorescence intensity, results were compared to untreated control cells (C) and expressed as the mean green fluorescence ± SD of the different samples.

To evaluate the mitochondrial ROS production induced by erionite fibres, cells were stained with the fluorescent dye MitoSOX™ Green, which is rapidly oxidized by mitochondrial superoxide producing a bright green fluorescence. Additionally, to evaluate whether the application of ROS scavengers could reduce mitochondrial oxidative stress, cells were pre-treated with 15 mM N-Acetyl-L-cysteine (NAC) for 2 h and then challenged with erionite fibres for 72 h. Images were obtained acquiring the green fluorescence (emission at 510 nm).

2.7. Gene expression profile of inflammatory cytokines

To evaluate the inflammatory potential of erionite, THP-1 monocytes were seeded in six-well plates at 500,000 cells/well, and once differentiated M0 macrophages were incubated with 50 μg/mL of erionite fibres for 7 or 14 d. Then, the gene expression profile of inflammatory mediators interleukin-1β (IL-1β, a.n. NM_000576.3), interleukin-6 (IL-6, a.n. NM_031168.2), interleukin-8 (IL-8, a.n. NM_000584.4), monocyte chemoattractant protein-1 (MCP-1, a.n. NM_002982) and tumour necrosis factor-alpha (TNF-α, a.n. NM_000594.4), was evaluated by qPCR relative to untreated control cells.

Total RNA was extracted using the NucleoSpin RNA, Mini kit (MACHEREY-NAGEL, Dueren, Germany) according to the manufacturer's instructions. The quality and quantity of RNA were analysed using a NanoDrop spectrophotometer (Nanodrop Technologies, Wilmington, DE, USA). The cDNA was synthesised from 500 ng of RNA by using a cDNA Synthesis Kit (biotechrabbit GmbH, Henningsdorf, Germany). Each PCR reaction was performed in 10 μL containing: 4x master mix (biotechrabbit GmbH, Henningsdorf, Germany), 0.2 μM of each primer and 2.5 ng of cDNA. All samples were analysed in triplicate. The following thermal conditions were used: initial denaturation at 95 °C for three minutes, followed by 45 cycles with denaturation at 95 °C for 15 s, and annealing and elongation at 60 °C for 60 s. The fluorescence was measured at the end of each elongation step and values were normalised to GAPDH (housekeeping gene, a.n. NM_002046) mRNA expression. All primers (Table S7) were designed using the Beacon Designer 7.0 software (Premier Biosoft International, Palo Alto, CA, USA) and obtained from TibMolBiol (Genova, Italy). Data analyses were obtained using the DNA Engine Opticon® 3 Real-Time Detection System Software program (3.03 version), and to calculate the relative gene expression compared to the untreated control sample, the comparative threshold Ct method was

Table 1
List of the analysed samples.

Name	Incubation media	Incubation time	pH
PRI (pristine)	-	-	-
H_2O pH 4.5	H_2O	7 d	4.5[c]
MGS pH 4.5[a]	MGS	28 d	4.5[c]
MGS pH 7.4[b]	MGS	1 d	7.4
Control PBS	PBS	1 d	7.4
Control RPMI	RPMI	1 d	7.4
ALF−14d	ALF	14 d	4.5
THP−1–1d	THP−1	1 d	-[d]
THP−1–7d	THP−1	7 d	-[d]
THP−1–14d	THP−1	14 d	-[d]
THP−1 PBS	PBS post THP−1	7 d in THP−1 + 1 d in PBS	7.4
THP−1 RPMI	RPMI post THP−1	7 d in THP−1 + 1 d in RPMI	7.4

[a] Sample analysed in [42].
[b] Sample analysed in [43].
[c] Adjusted with HCl.
[d] Not determined.

used with the Gene Expression Analysis for iCycler iQ Real Time Detection System software (Bio-Rad, Milan, Italy).

2.8. Statistical analysis

For PXRD data, the parameters obtained from the Rietveld refinement are the result of a least square procedures that minimize the difference between the calculated and the experimental diffraction patterns, in which the errors are calculated as a part of the refinement using singular value decomposition (SVD) of covariance matrix.

Statistical analysis was performed using one-way and two-way ANOVA plus Tukey's post-test (GraphPad Software, Inc., San Diego, CA, USA) when the number of investigated conditions was $n \geq 3$, while student's *t*-test was used when the number of investigated conditions was $n = 2$. Results with *p*-values < 0.05 were considered significant.

3. Results and discussion

3.1. Evaluation of erionite toxicity

Erionite toxicity on human THP-1-derived macrophages was evaluated by the MTT assay to assess the degree of cell damage caused by the working concentration used in the following experiments. The assay showed that, at the highest fibre concentration tested, 50 μg/mL, the mortality rate of macrophages ranged from ca. 20 % after 1 d to ca. 40 % after 14 d of incubation (Fig. 1a). Therefore, this concentration was considered optimal, since it could ensure a significant fibre uptake without excessive cell damage that would compromise the retrieval of *bona fide* internalised fibres.

By using 50 μg/mL concentration, a significant number of erionite fibres were found inside macrophages already after 1 d of incubation and the majority of fibres in the petri dishes were internalised after 7 and 14 d of exposure as displayed in the micrographs of Fig. 1b-c, respectively.

The list of analysed samples, including the corresponding labelling system, is shown in Table 1 whereas the composition of the used solutions (MGS: Mimicked Gamble's Solution; PBS: Phosphate Buffered Saline; RPMI cell medium: Roswell Park Memorial Institute cell medium; ALF: Artificial Lysosomal Fluid) are listed in Table S1. Experiments of incubation were duplicated, the second differing exclusively for a more prolonged washing of the fibres after retrieval from cells (see Methods for details).

3.2. Structural modifications

3.2.1. Pristine and control samples

The pristine sample used in this work, from Rome, Oregon, USA, is classified as erionite-Na, on the basis of its formula $K_{2.40}(Na_{3.30}Mg_{0.72}Ca_{0.35})[Al_{7.78}Si_{28.22}O_{72.04}] \bullet 29.75\ H_2O$ [43]. It is characterized by Si/Al of 3.63. The material contains ca. 4 wt% of chabazite, traces of quartz (ca. 0.1 wt%) and minor clays as impurities.

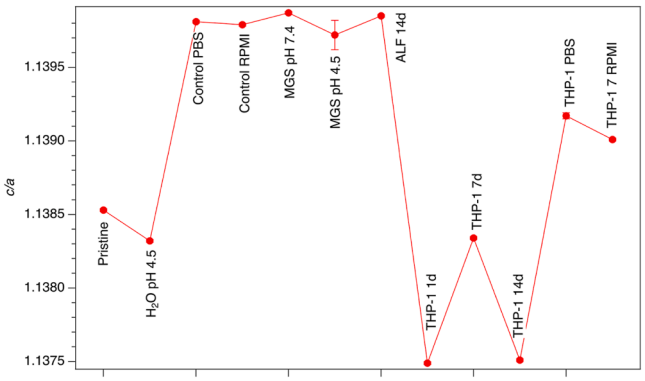

Fig. 2. Variation of the *c/a* ratio for the analysed samples.

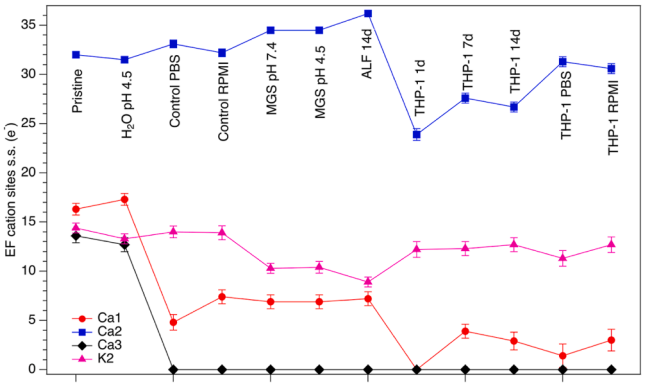

Fig. 3. Variation of s.s. at Ca1, Ca2, and Ca3 EF cation sites for the analysed samples.

The structure of PRI is identical to that reported in literature for samples from the same locality [43]. EF cations are allotted into the conventional Ca1 (mainly hosting Mg^{2+} and Na^{+}), Ca2 (Na^{+}), and Ca3 (Ca^{2+}+ Na^{+}) sites [42]. The additional K2 site, occluding the eight-ring opening at the walls of the erionite cavity, is partly occupied by K^{+} cations as in the case of samples having $K^{+} > 2$ a.p.f.u. Each one of the six OW sites (OW7–12) are approximately half occupied by H_2O (Tables S2-S4). Sample H_2O pH 4.5 is indistinguishable from PRI indicating that immersion in an acidic environment alone cannot alter in an appreciable way the structure of this zeolite. In fact, no modification of the site population of EF cation and OW sites was observed as well as of T-O bond distances (Table S5). Structural results are in perfect agreement with ICP-OES investigation showing a very small release of extra-framework cations from erionite fibres after immersion in water at 4.5 pH: the maximum content of released Na and K was ca. 2900 ppm and 400 ppm, respectively, whereas Ca and Mg were below the detection limit (< 50 ppb).

Control PBS and RPMI samples undertook very similar structural modifications. The unit cell stretches, as indicated by the significant increase of the *c/a* ratio (Fig. 2). This behaviour is likely induced by the significant release into the solution of Mg^{2+} and Ca^{2+} mainly allocated at Ca1 and Ca3, the latter being completely empty, following ionic exchange with Na^{+} ions present in the solution (Fig. 3). Moreover, no reduction of s.s. at K2 was observed, consistent with the presence of K^{+} cations in both PBS and RPMI (Table S1). The slightly reduced discharge of Ca1 occurring in RPMI as compared to PBS can be justified by the presence of Mg^{2+} and Ca^{2+} in the former solution, differently from the

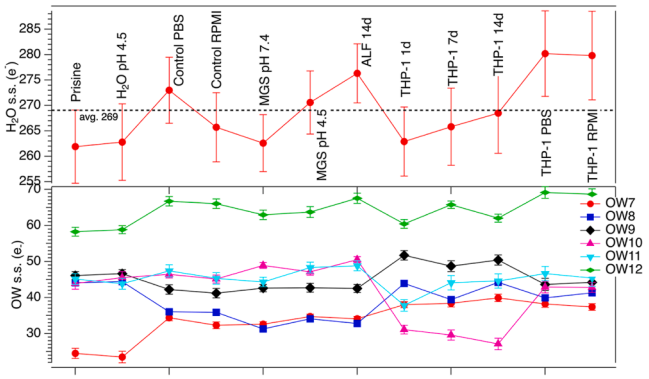

Fig. 4. Variation of s.s. at the individual OW sites (below) and variation of the total s.s at the OW sites (above) for the analysed samples.

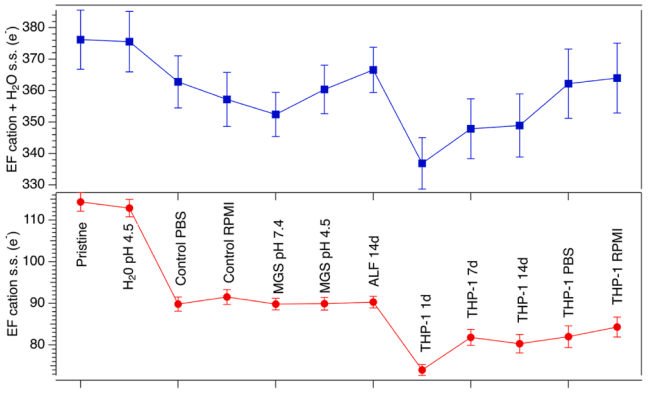

Fig. 5. Variation of the total s.s at the EF cation sites (below) and of the EF cation sites and of the total s.s. of OW plus EF cation sites (above) for the analysed samples.

latter.

Control PBS and RPMI samples showed structural adaptations comparable with those of the samples incubated in MGS [42,43], despite the very different incubation times (28 d for MGS pH 4.5, 1 d for MGS pH 7.4, 1 d for PBS and RPMI sample). Indeed, it has been shown that the EF cations are mostly exchanged within the first hour of incubation [42, 43]. The *c/a* ratio is very consistent for all four samples (Fig. 2), and close modifications of the s.s. at each OW and EF cation site were observed (Figs. 3 and 4), the only exception being K2 that decreases in the case of both MGS samples. This behaviour may be explained by a more abundant K release from the fibres driven by the absence of K^+ cations in MGS (Table S1). The total s.s. at the EF cation sites is significantly reduced with respect to PRI, but still in line with that observed for the control samples (Fig. 4).

Incubation in ALF produced slightly different structural modifications notwithstanding a *c/a* ratio close to that of control PBS and RPMI, and MGS incubated samples (Fig. 2). Despite a similar total s.s. of EF cations (ca. 90 e^-) ALF 14 d shows a minor reduction of s.s. at K2 counterbalanced by a small increase at Ca2, whereas Ca1 and Ca3 behave similarly (Fig. 3). Comparison of chemical analysis between pristine fibres and those after immersion in ALF (Table S6) shows that Na ions present in the solution are acquired by erionite following ion exchange with the extra-framework cations Ca, K and Mg, in perfect agreement with previous work [42,43]. Besides, ICP-OES analysis points to a preferential release of K (14712 ppm) and Ca (14873 ppm) and a minor release of Mg (4582 ppm) from the fibres during 14 days of incubation in ALF, in qualitative agreement with experiments of fibre incubation in MGS [42].

Fig. 5 indicates the reduction of the total s.s. allotted into the erionite cavity of the control samples, albeit associated to a relatively high standard deviation, mainly caused by the reduction of s.s. at the EF cation sites.

3.2.2. *THP-1 phagocytosed fibres*

Quantitative phase analysis (QPA) reveals a remarkably constant composition of the fibres retrieved at various time points from the macrophage intracellular environment that contain 3.65(5)-3.95(5) wt % of chabazite and 0.11(1)-0.14(1) wt% of quartz (Table S2). All samples, including the control ones, show a significant reduction of the clay content as compared to PRI, possibly caused by mechanical removal upon recovering of the fibres from the solutions or from the cells. The same effect may be invoked for the great reduction of calcite content and the complete removal of hydroxyapatite in THP-1–1d of the second set of samples as compared to the first one (Fig. S3). Early precipitation of calcite and apatite may be promoted by the fast and complete release of Ca^{2+} from erionite that has been experimentally measured by ICP-OES during incubation in MGS [42] and ALF. No degradation of the peak shape of erionite reflections was observed in the erionite fibres from the various experimental conditions testifying the absence of any detectable loss of crystallinity induced by permanence in the intracellular environment.

Cell parameters of THP-1 phagocytosed fibres indicate a generalized compression of the cell with respect to PRI, as indicated by the reduction of the *c*/a ratio (Fig. 2). The *c/a* ratio observed for THP-1–7d is slightly higher than that of THP-1–14d despite very marginal structural variations essentially confined to the OW sites population. This feature may be possibly attributed to a slightly different chemical composition of the pristine fibres used in the experiments. The refined values of the s.s. at the EF cation sites (Fig. 3) indicate the complete depletion of Ca1 and Ca3 and a relevant reduction of s.s. at Ca2 for THP-1–1d. In the case of THP-1–7d and −14d the s.s. increases somewhat and limited s.s. is observed at Ca1. We observe a very minor reduction of s.s. at K2 with respect to PRI, significantly smaller than that observed for ALF 14d. The minor release of K^+ ions into the cellular environment is reasonably hindered by the abundance of such cation inside the cells where the fibres are located.

The total EF cation s.s. decreases dramatically from 114(2) e^- of PRI to 73.8(13) e^- of THP-1–1d and to ca. 81 e^- in the case of increased incubation times (Fig. 5). Inspection of the SEM-EDS spectra further supports this result, revealing the absence of Ca together with the depletion of Mg and Na content for phagocytosed fibres after 1d and 14d incubation, with respect to the pristine fibres (Fig. S4). Moreover, K content seems to be comparable among all samples. Owing to the significantly different structural features shown by the control fibres immersed for 1 d in PBS and in RPMI cell medium, this is further proof that at least the great majority, if not all, of the recovered fibres were engulfed by THP-1 cells and not just lying in the culture media.

The decrease of s.s. at the EF cation sites experienced by the THP-1 phagocytosed fibres is coupled to a significant redistribution of s.s. at the various OW sites where H_2O is expected to be located. The most relevant variations are the increased s.s. at OW7 and the decrease at OW10 (Fig. 4). The remaining OW sites do not show significant modifications. In particular, the large decrease of s.s. at OW10 represents a peculiarity among the studied samples undergoing cation release.

Moreover, we repeated the PXRD measurements on the same THP-1 phagocytosed fibres, kept within the capillaries, after 6 months to detect the possible occurrence of kinetically driven rearrangement of EF cations and H_2O but the structural results were within 1σ of the original ones, indicating that the described configuration is stable (data not shown).

As above mentioned, we observed an increase of the s.s. of both EF cations and OW sites passing from THP-1–1d to −7d and −14d (Table S4). This is due to an increase of s.s. at both Ca1 and Ca2. Explanation to this behaviour may be linked to the very quick complete release of Ca from erionite structure to the biological environment that is

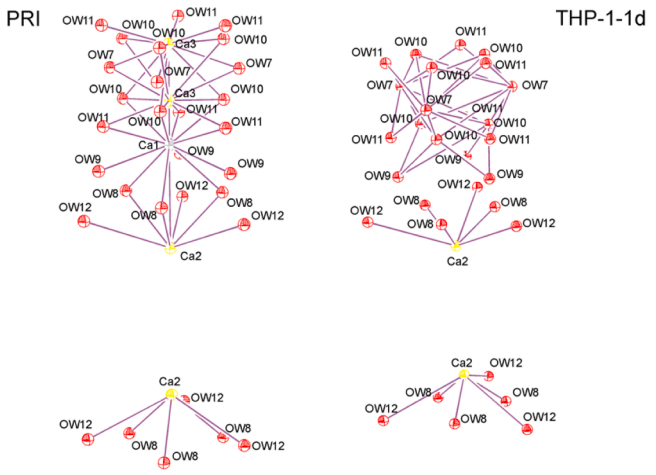

Fig. 6. Comparison of the erionite cage content of PRI and THP-1–1d. Figures drawn with Ortep-3 [72].

followed by a small re-equilibration process driven by the cations available within the lysosomal fluid and possibly by pH modifications. Under such aspect, the occurrence of minor calcite admixed to the erionite fibres in THP-1–1d seems to be counterintuitive according to the acidic pH of lysosomal fluid. An interpretation of this process will be provided in the following section.

The s.s. redistribution at OW sites of the fibres internalised by THP-1 macrophages is obtained without the occurrence of large displacement of the various sites (Table S4). However, the bonding system is different as, for example, only OW8, OW9, and OW12 are at bonding distance from Ca2. In the following we will discuss the structural features of THP-1–1d sample as representative of the effect of the interaction of the erionite fibres with THP-1 macrophages owing to the minor structural differences existing among the fibres residing into the cellular environment for longer periods (i.e., 7d and 14d). A comparison of the erionite cage content of PRI and THP-1–1d is sketched in Fig. 6. The most relevant displacement is represented by the vertical migration of OW8.

3.3. Interaction process of erionite fibres with control media and THP-1 macrophages

Both XRPD and SEM data showed that after internalization in THP-1 macrophages erionite fibres undertake a significant release of extra-framework cations and there is no evidence of Na^+ or K^+ binding from the cellular fluid. Protonation of oxygen atoms of the framework has been previously invoked to justify a small charge unbalance of ca. 1.5 e^- per formula unit (p.f.u.) occurring as a result of minor EF cation release in simulated lung fluids [37]. According to this picture, the proton is stabilized under the form of an OH group occupying one of the four oxygen atoms of the $[(Si,Al)O_4]$ tetrahedra of the framework and a "bridging" OH group is created having the potential to act as a Brønsted acid site. However, in the present case the expected charge mismatch is very large, as indicated by the significant reduction of s.s. at EF cation sites and an extended protonation of the framework without loss of crystallinity (not observed) seems implausible [65]. The occurrence of limited protonation at oxygen atoms of the framework was experimentally associated to the modification of <T-O> bond distances leading to a fictitious modification of the R=Si/(Si+Al) value (hereinafter referred to as R) calculated from the Jones' equation [66], that has been used as a reasonable qualitative estimate of the Si,Al population at T sites. However, it should be noted that this parameter shows an extreme sensitivity from small variations of bond distances. If we hypothesize that the very large reduction of s.s. at EF cation sites of the control samples (ca. 25 e^-) is entirely compensated by creating a corresponding number of OH bridges, they will represent ca. 1/3 of the oxygen atoms of the framework. This possibility seems not supported by the corresponding minimal variation of the <T1-O> (1.628–1.631 Å) and <T2-O> (1.644–1.650 Å) (Table S5).

As previously pointed out, THP-1–1d shows even a more dramatic reduction of s.s. at EF cation sites of ca. 40 e^-. The precipitation of calcite apparently suggests the abrupt increase of the pH in the internalization environment occurring in the first day. Conversely, its absence in fibres phagocytosed for longer times (i.e., 7 d to 14 d) together with the increase of s.s. at EF cation sites in the same samples, points to a subsequent restoration of the original acidic pH around the fibres. A possible explanation of the main mechanism of charge compensation is that the release of cations by the fibres (indicated as X for simplicity in the following) is largely counterbalanced by the uptake of hydronium ions from the cellular fluids according to one or more of the following simplified equations:

$$X^+_{(eri)} + 2H_2O \Leftrightarrow X^+_{(soln)} + H_3O^+_{(eri)} + OH^-_{(soln)} \quad (1)$$

$$X^{2+}_{(eri)} + 4H_2O \Leftrightarrow X^{2+}_{(soln)} + 2H_3O^+_{(eri)} + 2OH^-_{(soln)} \quad (2)$$

$$X^{2+}_{(eri)} + 2H_2O + X^+_{(soln)} \Leftrightarrow X^{2+}_{(soln)} + X^+_{(eri)} + H_3O^+_{(eri)} + OH^-_{(soln)} \quad (3)$$

In particular, the process outlined by Eq. 1) is well documented for several zeolite species, both as pristine or activated, immersed in water or aqueous solutions (e.g., FAU: [67] and references therein) and produces a pH increase in the solution caused by the fast release of OH^-. It is subsequently followed by a slow pH decrease arising from hydrolysis of the framework and partial release of hydronium ions [68,69]. The efficiency of the process strongly depends on the pH and is favoured by acidic conditions i.e. those typically occurring within lysosomes. It is worth noting that, in the present case, X represents K^+, Na^+, Ca^{2+}, and Mg^{2+} in the simplified equations.

Analysis of the T-O bond distances (Table S5) indicates that R significantly increases from PRI (0.793) to THP-1–1d (0.823) suggesting that this apparent increase could be caused by the onset of a different hydrogen bonding system with respect to PRI, induced by the uptake of H_3O^+ ions in place of H_2O, involving oxygen atoms of the framework possibly forming Zundel-like structures [70] or more complex hydration shells [71].

The subsequent pH reduction is coupled with the partial inversion of the process, as cations are uploaded by the fibres with simultaneous release of H_3O^+, explaining the increase of s.s. at both OW and EF cation sites observed for THP-1–7d and −14d (Fig. 5) as well as the progressive fictitious decrease of R with respect to THP-1–1d. Partial restoring of s.s. at Ca1 made us hypothesize a possible re-upload of Na^+ and/or Mg^{2+} from the cellular medium according to the reported cations preference for this site.

A visual comparison of the structure of PRI and THP-1–1d is illustrated in Fig. 6. In the case of THP-1–1d contacts among OW sites are drawn suggesting the occurrence of possible hydrogen bonds acting between H_2O and/or H_3O^+. It has been suggested that the high selectivity of aluminosilicate zeolites for hydronium ions must involve the three strong hydrogen bonds that each H_3O^+ should make with the oxygen atoms of the framework [67]. Analysis of the contacts between OW sites and oxygen atoms of the framework for THP-1–1d indicates that OW7, OW11, and OW12 are at potential hydrogen bond distance with three of them. Owing to the increase of s.s. at OW7 and OW12 with respect to PRI we can speculate that H_3O^+ should be preferentially allocated at those sites. Despite the minimal refilling of Ca1 observed for THP-1–7d and −14d, the structural details are substantially unchanged.

Analysis of the contacts between EF cation and OW sites and between OW and OW sites of THP-1–1d indicates the presence of several non-occurring bond distances caused by mutually excluding populations. Interpretation is rendered very complicated by the expected occurrence of cations at or near OW sites, and in general, of extended positional disorder.

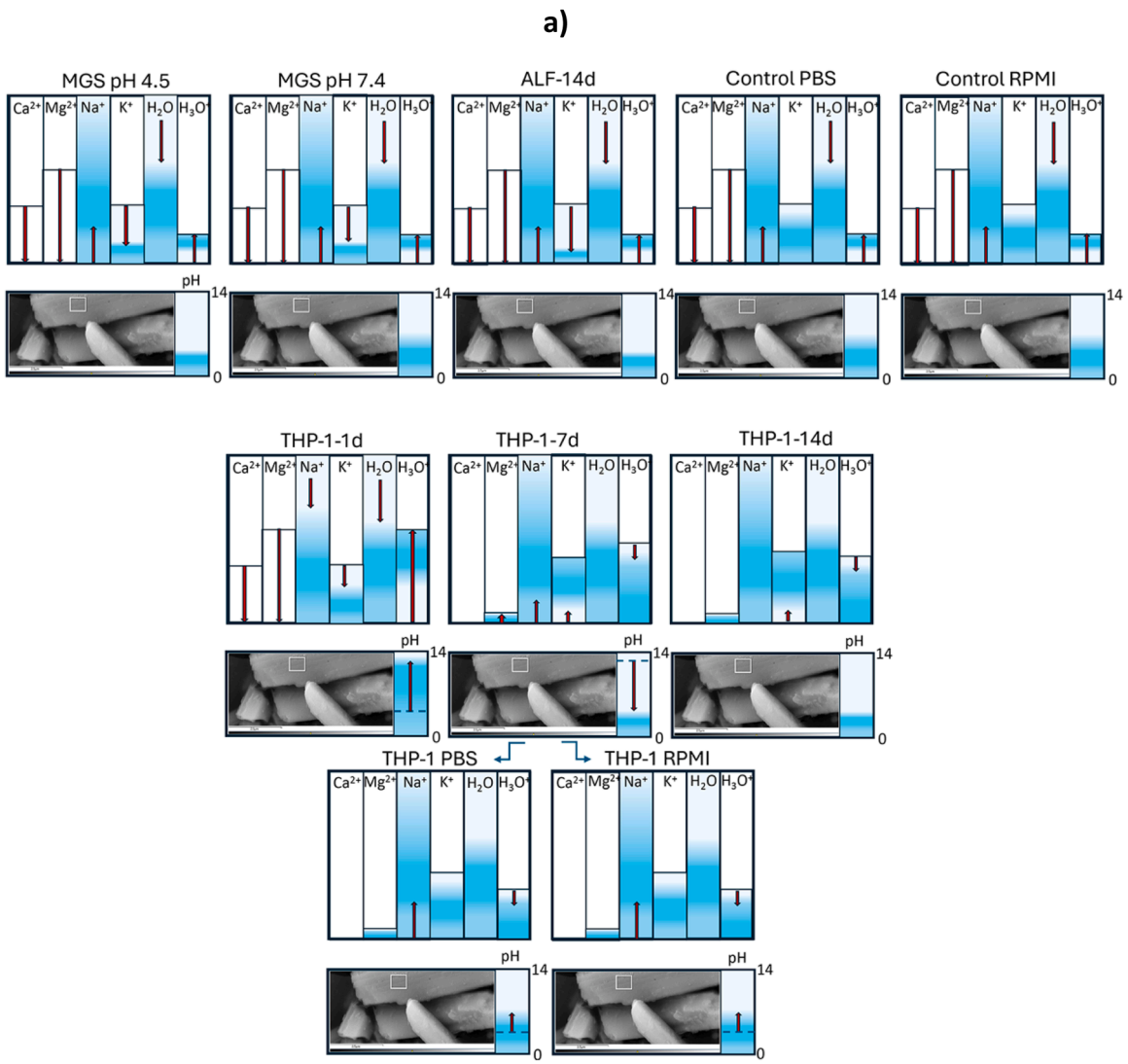

Fig. 7. Pictorial representation of the various processes undertaken by the fibres upon incubation as derived from structure refinements. a) Chemical variations from PRI of the various control samples. H_2O pH 4.5 not shown as no changes were observed. Arrows pointing up or down indicate, respectively, increase or reduction of the content as compared to PRI. b) Modification occurring in the phagocytosed erionite fibres retrieved from THP-1-derived macrophages. In the case of increasing time of incubation, variations refer to the previous time step. Differences for samples THP-1 PBS and RPMI are indicated with respect to THP-1–7d to monitor the possible reversibility of cation exchange processes after permanence of the fibres inside THP-1-derived macrophages and further release in the extracellular medium due to cell disruption in case of necrosis or apoptosis.

The Ca2 site is coordinated to 3 x OW8 at a very short 1.85(2) Å distance plus 3 x OW9, 3 x OW12, and 3 x O5 with distances lying in the 3.16–3.29 Å range. This very irregular coordination could be attributed, hypothesizing the short contact as a not occurring one, to the presence of K^+, similarly to K-exchanged erionite. However, this hypothesis is unsupported by the composition determined by SEM-EDS. Therefore, additional options were investigated to justify the occurrence of such anomalous coordination. First, we unsuccessfully tested the occurrence of s.s. at $x = 1/3, y = 2/3, z = 1/4$ corresponding to a site, located along the axis of the erionite cage, observed in the Tuzköy erionite sample and occupied by H_2O [73]. Subsequently, as in the case of erionite-K from Rome, Oregon [20], we slightly displaced off-axis Ca2 in the attempt to find a more suitable coordination for the cation. However, refinement was unstable despite very marginal improvement of the fit (results not reported). Nevertheless, clues of a more favourable coordination were observed as indicated by the lengthening of 2 x Ca2-OW8 to a more reasonable value of ca. 2.3 Å and the corresponding shortening below 3 Å of other contacts with OW9, OW12 and O5.

The K2 site, where K cations are allotted whenever exceeding 2 a.p.f.u., is coordinated by 2 x OW9 at a non-occurring 2.34(2) Å distance plus 2 x OW11, 2 x O4, 4 x O1, and 4 x OW8 with distances spread in the 3.09–3.35 Å range providing a 12-fold coordination perfectly fitting the presence of K. K2 and OW12 are mutually excluding because of the very short 0.931(16) Å contact.

Moreover, we observe a complex network mutually excluding populations among the various OW sites caused by small contacts close to 2 Å.

3.4. *Lysosomal and mitochondrial homeostasis disruption in erionite-phagocyting cells*

A pictorial representation of the various processes occurring on the phagocytosed fibres, as deduced from the structural analyses, is summarized in Fig. 7.

The fibres incubated for 7 d in THP-1 cells and subsequently exposed for 1 d to PBS and RPMI (THP-1 PBS and RPMI), mimicking the re-immersion in the extracellular environment after the release of fibres from dead macrophages, show a partial recovery of the s.s. at both OW

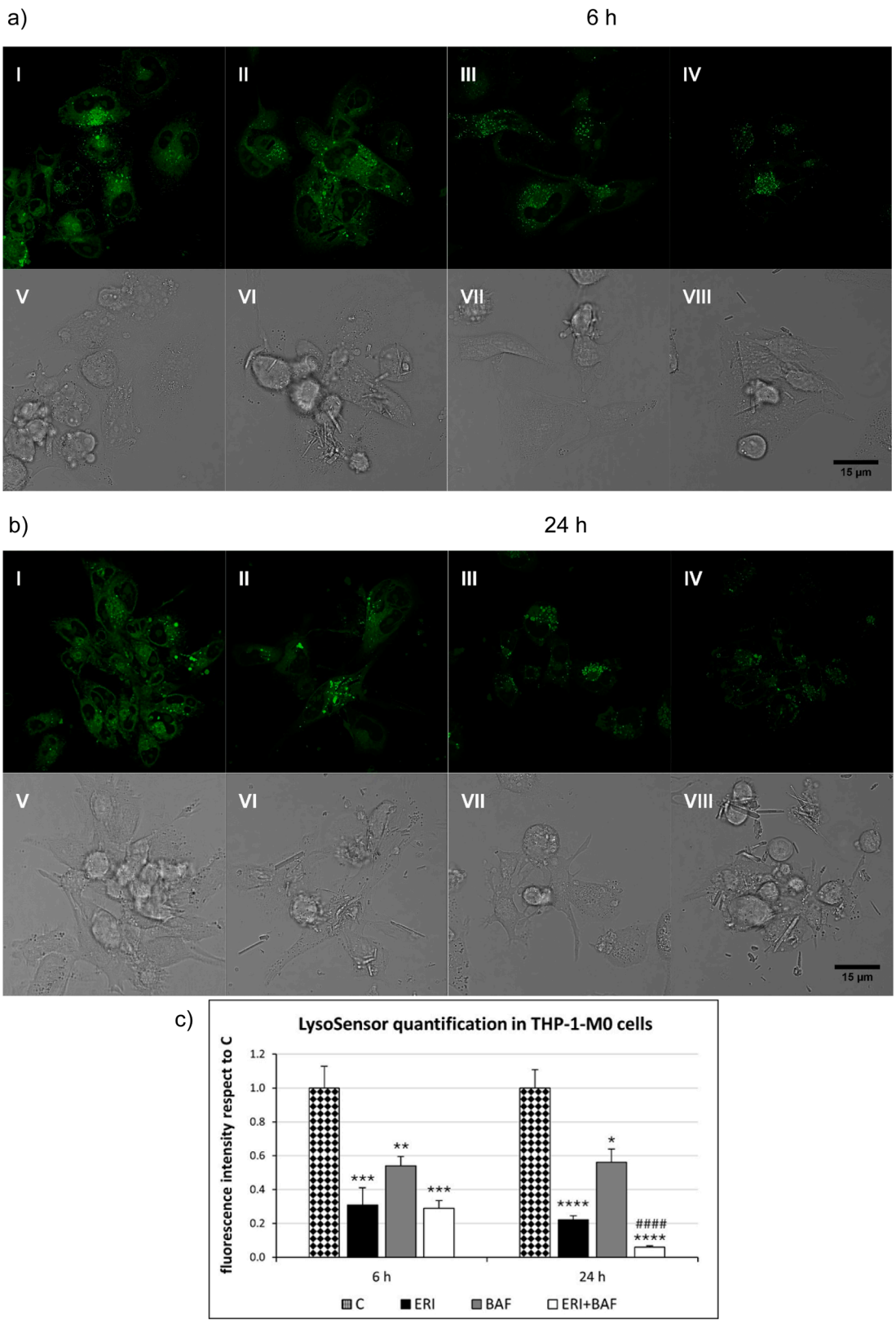

Fig. 8. Quantification of lysosomal pH dysregulation in THP-1 M0 cells. a-b) Representative confocal microscopy images (60x, plus 2x digital zoom) of erionite-treated THP-1-M0 macrophages (panel a 6 h; panel b 24 h, respectively) loaded with the fluorescent pH indicator LysoSensor™ Green DND-189. Panels I, V: control M0 cells; panels II, VI: erionite-treated M0 cells; panels III, VII: bafilomycin-treated M0 cells; panels IV, VIII: bafilomycin-treated erionite-exposed M0 cells. The black bar spans 15 μm. c) Quantification of the green fluorescence intensity measured in the confocal microscopy acquisitions respect to control untreated cells (C). Results are the mean ± SD of three different microphotographs and asterisks indicate significance in Tukey test (ANOVA $p < 0.0001$; Tukey vs. C, ****$p < 0.001$, ***$p < 0.005$, **$p < 0.01$, *$p < 0.05$; Tukey vs. ERI, ####$p < 0.001$, respectively).

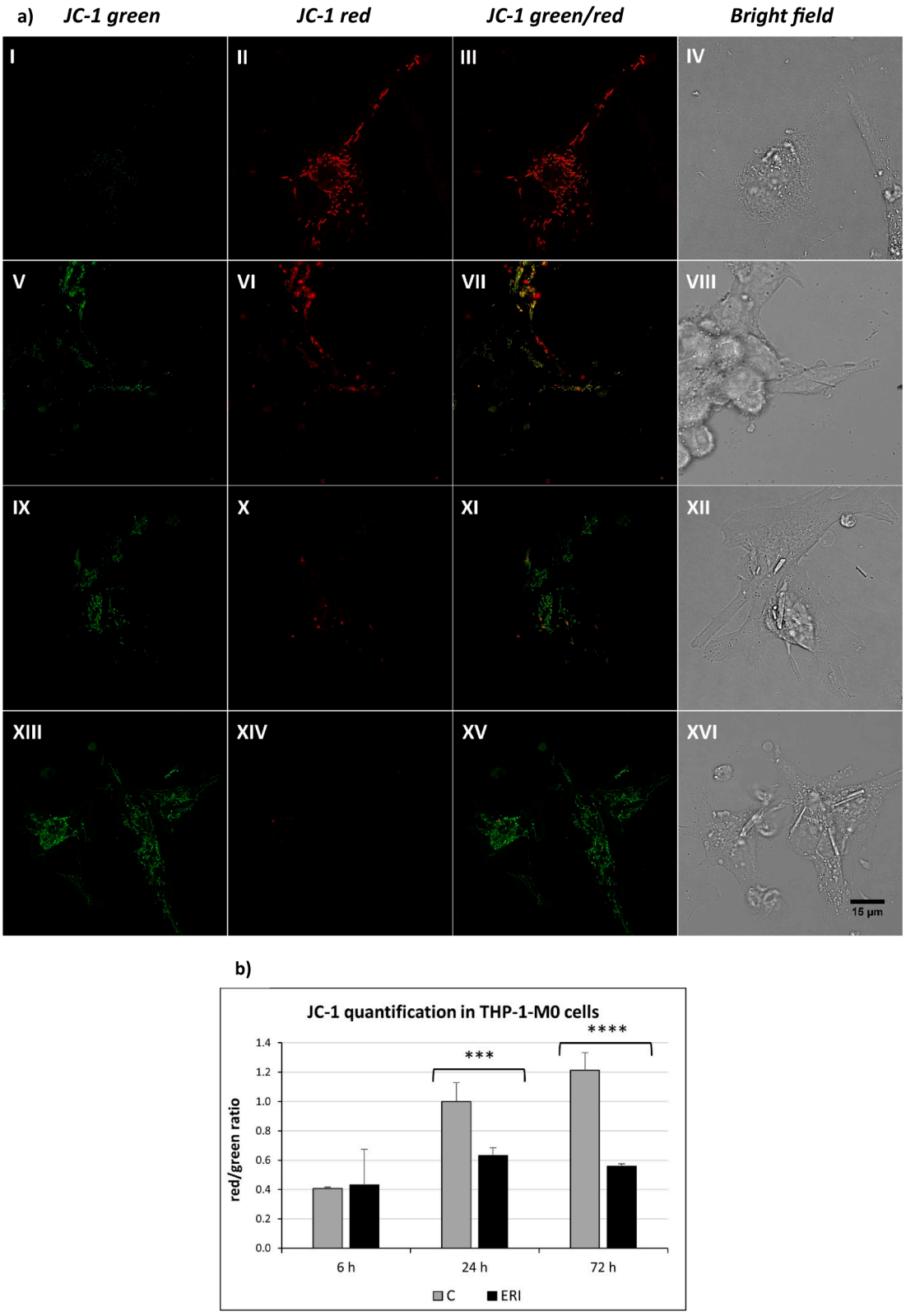

Fig. 9. Quantification of mitochondrial damage in THP-1 M0 cells. a) Representative confocal microscopy images (60x objective, 3x digital zoom) of erionite-treated or untreated THP-1-M0 macrophages loaded with the mitochondrial proton gradient (ΔΨ)-sensitive fluorescent dye JC-1. Panels I–IV: control M0 cells; panels V–VIII: erionite-treated M0 cells after 6 h incubation; panels IX–XII: erionite-treated M0 cells after 24 h; panels XIII–XIV: erionite-treated M0 cells after 72 h incubation. The black bar spans 15 μm. b) Quantification of the red/green fluorescence ratio measured in the confocal microscopy acquisitions. Results are the mean ± SD of five different microphotographs per each experimental condition and asterisks indicate significance in Tukey test (ANOVA $p < 0.001$; Tukey vs. C, ****$p < 0.001$, ***$p < 0.005$, respectively).

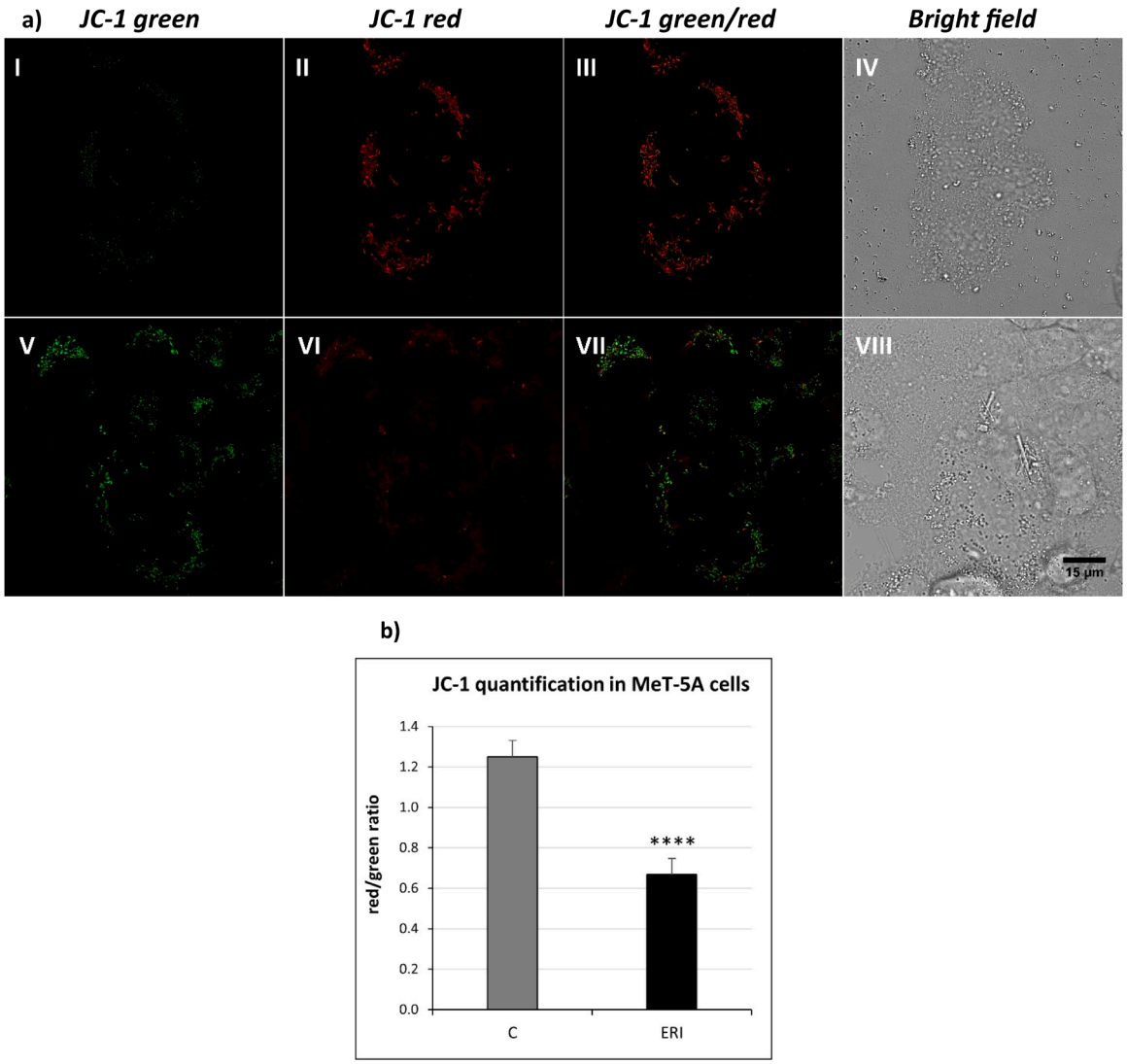

Fig. 10. Quantification of mitochondrial damage in MeT-5A cells. a) Representative confocal microscopy images (60x objective, 3x digital zoom) of erionite-treated or untreated MeT-5A cells loaded with the mitochondrial proton gradient (ΔΨ)-sensitive fluorescent dye JC-1. Panels I–IV: control MeT-5A cells; panels V–VIII: erionite-treated MeT-5A cells after 72 h incubation. The black bar spans 15 µm. b) Quantification of the red/green fluorescence ratio measured in the confocal microscopy acquisitions. Results are the mean ± SD of five different microphotographs per each experimental condition and asterisks indicate significance in student's -*t*-test (****$p < 0.001$).

sites and Ca2 indicating a relevant upload of cations from the media that, according to the allocation, should be essentially Na^+. The trend of structural convergence toward the corresponding control PBS and RPMI samples is clearly seen from scrutiny of the various graphs reported in Figs 2–5 indicating the possible extended reversibility of the ionic exchange process occurred inside THP-1 macrophages after phagocytosis. This would imply that at each ingestion/reingestion cycle in the lung environment, the erionite fibres would discharge the predominant Na^+ and/or K^+ cations in exchange for the abundant H_3O^+ inside the acidic phagolysosomes and subsequently recharge them when released again into the neutral, sodium-rich extracellular milieu, after macrophage cell death. An important consequence of this phenomenon would be that at each macrophage cell reingestion the fibres regain one of erionite toxicity characteristics in a perpetual way. In fact, the H_3O^+ upload on the fibre surface could cause a significant alteration of the acidic pH of the phagolysosomes that would be rebalanced by the hyperactivation of the ATP-dependent proton pumps in the organelle membranes with an energetic cost for the cells possibly affecting the mitochondrial and cell homeostasis. A similar conclusion was also suggested by Raneri and coworkers [47], whose study hypothesized a mitochondrial disfunction for the cells internalising erionite fibres, in that case attributed to an abnormal decrease of the intracellular Ca^{2+} concentration in the days after the phagocytosis, affecting calcium-dependent mitochondrial enzymes activity. Thus, to gain more insight also on the possible role of lysosome dysfunction in erionite cytotoxicity, we decided to investigate the pH basification of lysosomes in erionite-phagocyting THP-1 M0 macrophages through the pH-sensitive LysoSensor™ Green fluorescent dye. This specific lysosomal probe shows maximum fluorescence at an acidic pH (pK_a <5.2) with a decrease of fluorescence proportional to the increase of the organelle pH. The images in Fig. 8a-b indeed demonstrate that both at 6 and 24 h incubation, macrophages with engulfed erionite fibres show a significant green fluorescence decrease (i.e. pH basification) in the lysosomes as compared to control, untreated cells, as also quantified in the graph in Fig. 8c (black bars, 70 % and 80 % decrease at 6 h and at 24 h, respectively). Subsequently, we investigated the role of the lysosomal proton pumps in counterbalancing the lysosome basification in erionite-engulfed cells by use of Bafilomycin A1, an effective vacuolar-type ATP-dependent proton pump inhibitor, that is widely used as a pharmacological tool in many *in vitro* research applications [74]. Thus, Bafilomycin A1 was added to both untreated and

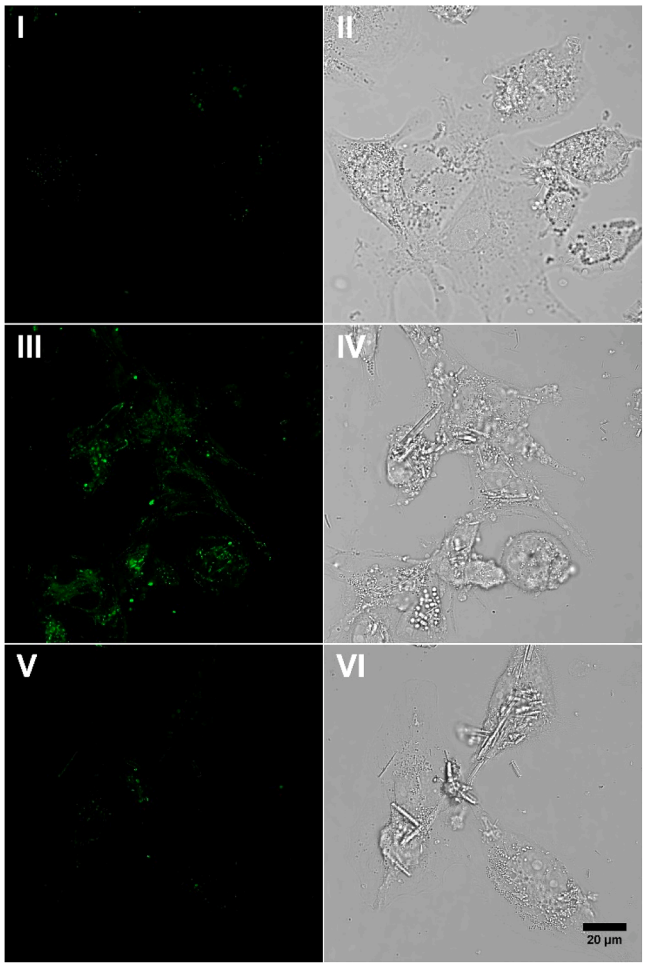

Fig. 11. Quantification of mitochondrial ROS in THP-1 M0 cells. Representative confocal microscopy images (60x objective, 2x digital zoom) of erionite-treated or untreated THP-1-M0 macrophages loaded with the mitochondrial ROS-sensitive fluorescent dye MitoSOX™ Green. Panels I–II: control M0 cells; panels III–IV: erionite-exposed M0 cells after 72 h incubation; panels V–VI: NAC-treated (15 mM) and erionite-exposed M0 cells after 72 h incubation. The black bar spans 20 μm.

erionite-treated macrophages and the shift of the lysosomal pH was again evaluated after 6 and 24 h. The results showed that, similarly to erionite alone, Bafilomycin A1 treatment led to a significant lysosomal pH increase in macrophages at both time points (Fig. 8a-b) as compared to control cells indicating the effective proton pump blockade (Fig. 8c, grey bars, 45 % fluorescence decrease at both time points). But more importantly, we observed that with the passing of time (from 6 to 24 h), the concomitant treatment of Bafilomycin and erionite fibres caused a drastic lysosomal fluorescence decrease (Fig. 8c, white bar, 90 % decrease) indicating a significant basification of the lysosomes (i.e. pH >5.2). Thus, these results strengthen the hypothesis that, indeed phagocytosed erionite fibres lead to an increase of the lysosomal pH in the cells already in the first 24 h, which is very much evident in the presence of the specific proton pump blocker Bafilomycin A1 disabling the rebalancing of the organelle acidic pH by the proton pumps.

Given these results, as well as those of Raneri et al. [47], likely a great deal of erionite toxicity after cellular ingestion would be centred on the mitochondria, with the compromission of cell respiration mechanisms and of the ATP production rate. Most importantly, this phenomenon would also occur in mesothelial cells which have a documented fibre-uptake capacity [74], altering the cell homeostasis by ATP depletion and contributing to the onset of biochemical conditions favouring cell transformation and mesothelioma development [75]. To shed light on the hypothesis of the cell mitochondrial suffering and function compromission after erionite fibre internalization, both THP-1 M0 macrophages and MeT-5A human mesothelial cells were incubated with erionite fibres up to 72 h and then their mitochondrial inner membrane potential was measured by use of the mitochondrial proton gradient (ΔΨ)-sensitive fluorescent probe JC-1 (Figs. 9 and 10, respectively). This ratiometric probe switches from a red to a green fluorescence emission inside mitochondria because of the inner membrane potential depolarization, indicating a compromission of the electron transport chain and of the ATP-synthase activity in the organelles [64]. Indeed, in THP-1 M0 macrophages a significant mitochondrial membrane depolarization was observed after erionite fibre exposure at 24 and 72 h incubation (Fig. 9a-b) leading to a 40 % and 50 % ΔΨ decrease in cells with phagocytosed fibres, respectively, as compared to control, healthy cells (Fig. 9b). A similar behaviour, confirming the severity of erionite mitochondrial toxicity, was observed also in MeT-5A human mesothelial cells, where again a 50 % ΔΨ decrease was observed in cells with internalised fibres as compared to controls (Fig. 10a-b), in this case after a 72 h exposure, being the 24 h incubation insufficient to highlight the mitochondrial membrane depolarization in these cells (not shown). To gain further insight into the mitochondrial stress in erionite-phagocyting M0 macrophages, the mitochondrial ROS

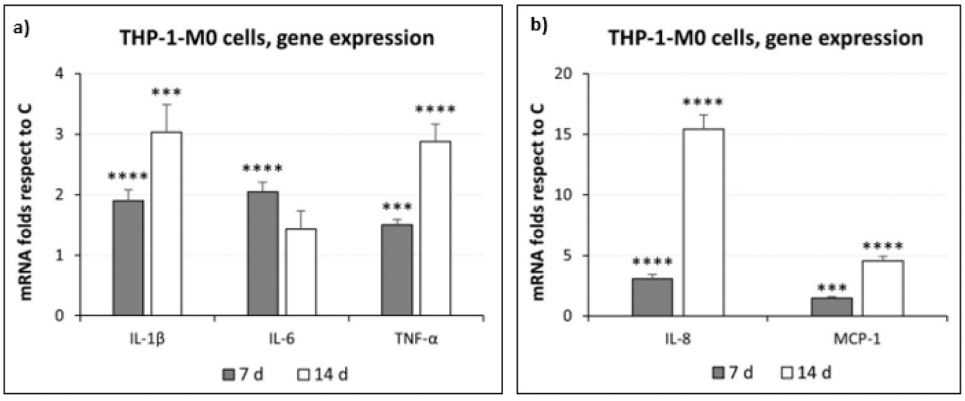

Fig. 12. Gene expression of inflammatory mediators measured by qPCR analysis. a) Gene expression of IL-1β, IL-6 and TNF-α in THP-1-M0 macrophages treated with 50 μg/mL of erionite fibres for 7 d (grey bars) or 14 d (white bars). Data are normalised to the GAPDH housekeeping gene and expressed as mRNA fold increase compared to untreated, control cells (C). Asterisks indicate significance in Tukey test (ANOVA $p < 0.00001$, Tukey vs C ****$p < 0.001$, ***$p < 0.005$, respectively). b) Gene expression of IL-8 and MCP-1 measured in THP-1-M0 macrophages in the same conditions as (a). Asterisks indicate significance in Tukey test (ANOVA $p < 0.0001$, Tukey vs C ****$p < 0.001$, ***$p < 0.005$, respectively).

production was also analysed with the specific superoxide anion-sensitive MitoSOX™ Green fluorescent probe at 24 and 72 h. Indeed, the results of these analyses show that, although at 24 h no significant mitochondrial ROS production was yet observable (Fig. S6), at 72 h incubation the mitochondrial ROS were indeed significantly increased in erionite-engulfed macrophages as compared to untreated cells (Fig. 11). Since ROS production has well-known detrimental cyto- and genotoxic effects [49–51], we decided to evaluate the impact of N-acetyl-L-cysteine (NAC), a well-known ROS inhibitor [76], on the mitochondrial ROS production induced in macrophages following erionite phagocytosis. The results of this investigation (Fig. 11) showed that, indeed, the use of NAC is effective in significantly reducing the mitochondrial ROS exacerbated production in erionite-engulfed macrophages, indicating a possible use of this drug in alleviating the erionite pulmonary toxic effects in exposed subjects.

As a results of the above-mentioned chain of events in erionite-phagocyting cells (i.e., lysosome basification → lysosome proton pumps hyperactivation → higher ATP consumption → mitochondrial suffering), cells would then begin to manifest cyto-, geno-toxic, and pro-inflammatory effects [50]. Furthermore, with the perpetration of fibre ingestion-reingestion cycles, erionite would be able to reset its H_3O^+ uptake capacity at each cycle by an intermediate extracellular passage (see Fig. 7), leading to chronic inflammation. To obtain indications on the development of chronic inflammation and possibly cancer onset, the gene expression profile of inflammatory cytokines was evaluated in erionite-exposed THP-1 macrophages at the longest incubation times (i.e. 7 and 14 d) mimicking *in vitro* a semi-chronic inflammation, and the results are shown in Fig. 12. It is possible to notice that the main inflammatory mediators (e.g. IL-1β, IL-6, TNF-α, IL-8 and MCP-1), also usually associated with cancer development by exacerbating the local inflammation of the tissue, are overexpressed in erionite-treated cells at both time points, with a further significant increase of the gene expression from day 7 to day 14 for all mediators (except IL-6). These data indicate that erionite-engulfed macrophages increase the production of inflammatory mediators with the passing of time other than diminishing them, due for example to the cytotoxic effect of erionite that could impair the intracellular gene expression machinery. This type of cellular response observed after two weeks of incubation *in vitro* is an indication that phagocytosed erionite may lead to a chronic inflammatory state also *in vivo*, which is in many cases prodromic to cancer development as attested by a vast literature on the topic (for a review see [77]).

Overall, our data seem to confirm that, although in an unexpected way, erionite ion exchanging capacity indeed has a role in the cytotoxicity of this mineral which is surprisingly exerted by sequestering H_3O^+ ions from the fluid of the lysosomes, increasing the pH of the organelles. Consequently, the increased activity of the membrane proton pumps of the organelle to restore the acidic pH, lead to a significant ATP expenditure and mitochondrial suffering in the cells, definitely compromising the cellular functions and homeostasis.

4. Conclusions and implications

In this work the crystal chemical and crystal structural modifications of erionite fibres following incubation in human THP-1 macrophages was investigated at different exposure times (1, 7, and 14 days) and correlated with the observed cellular response. The mineralogical investigation has shown for the first time that the fibres internalised by those cells during the first day of incubation (sample THP-1–1d) undertook a large release of extra-framework cations (i.e., Na^+, Ca^{2+}), counterbalanced by a significant sequestration of hydronium ions from lysosomes. It must be pointed out that semiquantitative chemical analyses by TEM/EDS of erionite fibres from bronchoalveolar lavage fluid (BALF) of Tuzköy villagers indicated significant loss of cations with respect to the mean composition of the erionite fibres sampled in the soils confirming the onset of the observed process also *in vivo* [78]. The composition of the PRI sample is close to that of the fibres found in the soil of Tuzköy and its dimensional heterogeneity compares favourably with that of the fibres recovered from BALF. Furthermore, consistently with present results, Raneri and coworkers [47] reported a substantial Na^+ increase in the cell cytoplasm in the first 24 h of phagocytosis of erionite fibres inside THP-1 macrophages. This increase, other than due to the activation of Ca^{2+}/Na^+ plasma membrane exchanger, necessary to restore the increased cytoplasmic Ca^{2+} concentration stimulating the phagocytosis [79], can be also related with the significant Na^+ release from the internalised fibres. The uptake of H_3O^+ by erionite fibres provokes the pH basification of lysosomes in macrophages, as demonstrated through the pH-sensitive LysoSensor™ Green fluorescent dye. This event is further confirmed by the occurrence of calcite and apatite in THP-1–1d sample. Calcite precipitation occurs in nature in a wide range of slightly to highly alkaline environments [80] and bioapatite precipitates from extracellular fluid whose pH is about 7 [81]. Besides, at pH of 4.5, such as might occur within a macrophage phagolysosome, hydroxyapatite is undersaturated and it is not predicted to precipitate [82]. Accordingly, the absence of calcite and apatite in samples following incubation for 7 and 14 days in macrophages suggests that the pH may regain the original acidity, dissolving both mineral phases. Following the lysosomal pH basification, a hyperactivation of the ATP-dependent proton pumps in the organelle membranes to restore the physiological acidic pH was observed, with significant energy expenditure for the cell, as evidenced by cell mitochondrial stress and function compromission. Notably, overexpression of the main inflammatory cytokines (e.g. IL-1β, IL-6, TNF-α, IL-8 and MCP-1) in erionite-exposed THP-1 macrophages at the longest incubation times (i.e. 7 and 14 days) indicated development of chronic inflammation, possibly leading to carcinogenesis and tumour progression *in vivo*.

Environmental implication

Erionite is a ubiquitous natural zeolite, often occurring with fibrous habit, whose strong tumorigenic activity to humans has been certified by its inclusion in the Group 1 Human-Carcinogenic list by the International Agency for Research on Cancer. This paper represents the first attempt to conjugate the analysis of the effects of fibre uptake by macrophages on both cells and fibres for disclosing the possible reasons of erionite toxicity.

CRediT authorship contribution statement

Montereali Maria Rita: Formal analysis, Data curation. **Arrizza Lorenzo:** Formal analysis, Data curation. **Passalacqua Mario:** Investigation, Formal analysis, Data curation, Conceptualization. **Mirata Serena:** Writing – review & editing, Writing – original draft, Investigation, Formal analysis, Data curation, Conceptualization. **Scarfì Sonia:** Writing – review & editing, Writing – original draft, Investigation, Data curation, Conceptualization. **Ballirano Paolo:** Writing – review & editing, Writing – original draft, Supervision, Project administration, Investigation, Funding acquisition, Formal analysis, Conceptualization. **Pacella Alessandro:** Writing – review & editing, Writing – original draft, Investigation, Data curation, Conceptualization. **Di Carlo Maria Cristina:** Formal analysis, Data curation.

Declaration of Competing Interest

The authors declare the absence of competing interests.

Acknowledgments

This study was carried out within the RETURN Extended Partnership and received funding from the European Union Next-Generation EU (National Recovery and Resilience Plan – NRRP, Mission 4, Component 2, Investment 1.3 – D.D. 1243 2/8/2022, PE0000005).

Appendix A. Supporting information

Supplementary data associated with this article can be found in the online version at doi:10.1016/j.jhazmat.2025.137546.

Data availability

Data will be made available on request.

References

[1] Passaglia, E., Sheppard, R.A., 2001. The crystal chemistry of zeolites. In: Bish, D.L., Ming, D.W. (Eds.), Natural zeolites: Occurrence, properties, applications. Reviews in Mineralogy & Geochemistry 45. Mineralogical Society of America. Geochemical Society, Washington DC, USA, pp. 69–116.

[2] McCusker, L.B., Olson, D.H., Baerlocher, C., 2007. Sixth revised Edition, Elsevier on behalf of the Structure Commission of the. Atlas of Zeolite Framework Types. International Zeolite Association, pp. 128–129.

[3] Kawahara, A., Curien, H., 1969. La structure crystalline de l'érionite. B Soc Fr Miner Cr 92, 250–256.

[4] Coombs, D.C., Alberti, A., Armbruster, T., Artioli, G., Colella, C., Galli, E., Grice, J. D., Liebau, F., Mandarino, J.A., Minato, H., Nickel, E.H., Passaglia, E., Peacor, D.R., Quartieri, S., Rinaldi, R., Ross, M., Sheppard, R.A., Tillmanns, E., Vezzalini, G., 1997. Recommended nomenclature for zeolite minerals: report of the subcommittee on zeolites of the International Mineralogical Association, commission on new minerals and mineral names. Can Miner 35, 1571–1606.

[5] Wise, W.S., Tschernich, R.W., 1976. The chemical compositions and origin of the zeolites offretite, erionite, and levyne. Am Miner 61, 853–863.

[6] Passaglia, E., Artioli, G., Gualtieri, A., 1998. Crystal chemistry of the zeolites erionite and offretite. Am Miner 83, 577–589.

[7] Gualtieri, A., Artioli, G., Passaglia, E., Bigi, S., Viani, A., Hanson, J.C., 1998. Crystal structure-crystal chemistry relationships in the zeolites erionite and offretite. Am Miner 83, 590–600.

[8] Gottardi, G., Galli, E., 1985. Natural zeolites. Springer-Verlag, Heidelberg, pp. xii + 409.

[9] Meier, W.M., Groner, M., 1981. Zeolite structure type EAB: crystal structure and mechanism for the topotactic transformation of the Na, TMA form. J Solid State Chem 37, 204–218. https://doi.org/10.1016/0022-4596(81)90086-4.

[10] Smith, J.V., Bennett, J.M., 1981. Enumeration of 4-connected 3-dimensional nets and classification of framework silicates: the infinite set of ABC-6 nets; the Archimedean and 6-related nets. Am Miner 66, 777–788.

[11] Smith, J.V., Rinaldi, F., Dent Glasser, L.S., 1963. Crystal structures with a chabazite framework. II. Hydrated Ca-chabazite at room temperature. Acta Crystallogr 16, 45–53. https://doi.org/10.1107/S0365110X63000074.

[12] Rüdinger, B., Tillmanns, E., Hentschel, G., 1993. Bellbergite – a new mineral with the structure type EAB. Min Pet 48, 147–152.

[13] Ballirano, P., Merlino, S., Bonaccorsi, E., Maras, A., 1996. The crystal structure of liottite, a six-layer member of the cancrinite group. Can Miner 34, 1021–1030.

[14] Staples, L.W., Gard, J.A., 1959. The fibrous zeolite erionite: its occurrence, unit cell, and structure. Miner Mag 32, 261–281. https://doi.org/10.1180/minmag.1959.032.247.01.

[15] Gard, J.A., Tait, J.M., 1973. Refinement of the crystal structure of erionite. In: Uytterhoeven, J.B. (Ed.), Proceedings of the Third International Conference on Molecular Sieves, 1973. Leuven University Press, Leuven, Belgium, p. 94.

[16] Mortier, W.J., 1982. Compilation of extra framework sites in zeolites. Butter Sci Ltd Struct Comm Int Zeolite Assoc 71.

[17] Alberti, A., Martucci, A., Galli, E., Vezzalini, G., 1997. A reexamination of the crystal structure of erionite. Zeolites 19, 349–352. https://doi.org/10.1016/S0144-2449(97)00102-4.

[18] Ballirano, P., Bloise, A., Gualtieri, A.F., Lezzerini, M., Pacella, A., Perchiazzi, N., Dogan, M., Dogan, A.U., 2017. The crystal structure of mineral fibres. In: Gualtieri, A.F. (Ed.), Mineral Fibres: Crystal Chemistry, Chemical-Physical Properties, Biological Interaction and Toxicity. EMU Notes in Mineralogy 18. European Mineralogical Union and Mineralogical Society of Great Britain & Ireland, London, pp. 17–64. https://doi.org/10.1180/EMU-notes.18.2.

[19] Schlenker, J.L., Pluth, J.J., Smith, J.V., 1977. Dehydrated natural erionite with stacking faults of the offretite type. Acta Crystallogr B 33, 3265–3268. https://doi.org/10.1107/S0567740877010784.

[20] Ballirano, P., Andreozzi, G.B., Dogan, M., Dogan, A.U., 2009. Crystal structure and iron topochemistry of erionite-K from Rome, Oregon, U.S.A. Am Miner 94, 1262–1270. https://doi.org/10.2138/am.2009.3163.

[21] Ballirano, P., Cametti, G., 2012. Dehydration dynamics and thermal stability of erionite-K: Experimental evidence of the "internal ionic exchange" mechanism. Micro Mesopor Mater 163, 160–168. https://doi.org/10.1016/j.micromeso.2012.06.059.

[22] Coffin, D.L., Cook, P.M., Creason, J.P., 1992. Relative mesothelioma induction in rats by mineral fibers: comparison with residual pulmonary mineral fiber number and epidemiology. Inhal Toxicol 4, 273–300. https://doi.org/10.3109/08958379209145671.

[23] IARC, 1987. IARC Monographs on the evaluation of the carcinogenic risk to humans. Silica some Silic 42, 225–239.

[24] IARC, 2011. IARC Monographs on the evaluation of the carcinogenic risk to humans. Arsen Met Fibres Dusts 100C, 311–316.

[25] Baris, Y.I., Sahin, A.A., Ozesmi, M., Kerse, I., Ozen, E., Kolacan, B., Altinörs, M., Göktepeli, A., 1978. An outbreak of pleural mesothelioma and chronic fibrosing pleurisy in the village of Karain/Urgup in Anatolia. Thorax 33, 181–192. https://doi.org/10.1136/thx.33.2.181.

[26] Carbone, M., Baris, Y.I., Bertino, P., Brass, B., Comertpay, S., Dogan, A.U., Gaudino, G., Jube, S., Kanodia, S., Partridge, C.R., Pass, H.I., Rivera, Z.S., Steele, I., Tuncer, M., Way, S., Yang, H., Miller, A., 2011. Erionite exposure in North Dakota and Turkish villages with mesothelioma. Proc Natl Acad Sci 108, 13618–13623. https://doi.org/10.1073/pnas.110588710.

[27] Carbone, M., Yang, H., Pass, H.I., Krausz, T., Testa, J.R., Gaudino, G., 2013. BAP1 and cancer. Nat Rev Cancer 13, 153–159. https://doi.org/10.1038/nrc3459.

[28] Wagner, J.C., Skidmore, J.W., Hill, R.J., Griffiths, D.M., 1985. Erionite exposure and mesotheliomas in rats. Br J Cancer 51, 727–730. https://doi.org/10.1038/bjc.1985.108.

[29] Hill, R.J., Edwards, R.E., Carthew, P., 1990. Early changes in the pleural mesothelium following intrapleural inoculation of the mineral fibre erionite and the subsequent development of mesotheliomas. J Exp Pathol 71, 105–118.

[30] Carthew, P., Hill, R.J., Edwards, R.E., Lee, P.N., 1992. Intrapleural administration of fibres induces mesothelioma in rats in the same relative order of hazard as occurs in man after exposure. Hum Exp Toxicol 11, 530–534. https://doi.org/10.1177/096032719201100615.

[31] Coffin, D.L., Cook, P.M., Creason, J.P., 1992. Relative mesothelioma induction in rats by mineral fibers: comparison with residual pulmonary mineral fiber number and epidemiology. Inhal Toxicol 4, 273–300. https://doi.org/10.3109/08958379209145671.

[32] Carbone, M., Yang, H., 2012. Molecular pathways: targeting mechanisms of asbestos and erionite carcinogenesis in mesothelioma. Clin Cancer Res 18, 598–604. https://doi.org/10.1158/1078-0432.CCR-11-2259.

[33] Gualtieri, A.F., 2023. Journey to the centre of the lung. The perspective of a mineralogist on the carcinogenic effects of mineral fibres in the lungs. J Hazard Mat, 130077. https://doi.org/10.1016/j.jhazmat.2022.130077.

[34] Matassa, R., Familiari, G., Relucenti, M., Battaglione, E., Downing, C., Pacella, A., Cametti, G., Ballirano, P., 2015. A deep look into erionite fibres: an electron microscopy investigation of their self-assembly. Sci Rep 5, 16757. https://doi.org/10.1038/srep16757.

[35] Eborn, S.K., Aust, A.E., 1995. Effect of iron acquisition on induction of DNA single-strand breaks by erionite, a carcinogenic mineral fiber. Arch Biochem Biophys 316, 507–514. https://doi.org/10.1006/abbi.1995.1067.

[36] Ballirano, P., Pacella, A., Cremisini, C., Nardi, E., Fantauzzi, M., Atzei, D., Rossi, A., Cametti, G., 2015. Fe (II) segregation at a specific crystallographic site of fibrous erionite: a first step toward the understanding of the mechanisms inducing carcinogenicity. Micro Mesopor Mater 211, 49–63. https://doi.org/10.1016/j.micromeso.2015.02.046.

[37] Pacella, A., Fantauzzi, M., Atzei, D., Cremisini, C., Nardi, E., Montereali, M.R., Rossi, A., Ballirano, P., 2017. Iron within the erionite cavity and its potential role in inducing its toxicity: evidences of Fe (III) segregation as extra-framework cation. Micro Mesopor Mater 237, 168–179. https://doi.org/10.3390/min8020036.

[38] Fach, E., Kristovich, R., Long, J., Waldman, W.J., Dutta, P.K., Williams, M., 2003. The effect of iron on the biological activities of erionite and mordenite. Environ Int 29, 451–458. https://doi.org/10.1016/S0160-4120(02)00193-9.

[39] Gualtieri, A.F., Gandolfi, N.B., Pollastri, S., Pollok, K., Langenhorst, F., 2016. Where is iron in erionite? A multidisciplinary study on fibrous erionite-Na from Jersey (Nevada, USA). Sci Rep 6, 1–11. https://doi.org/10.1038/srep37981.

[40] Bononi, A., Giorgi, C., Patergnani, S., Larson, D., Verbruggen, K., Tanji, M., Pellegrini, L., Signorato, V., Olivetto, F., Pastorino, S., Nasu, M., Napolitano, A., Gaudino, G., Morris, P., Sakamoto, G., Ferris, L.K., Danese, A., Raimondi, A., Tacchetti, C., Kuchay, S., Pass, H.I., Affar, E.L., Yang, H., Pinton, P., Carbone, M., 2017. BAP1 regulates IP3R3-mediated Ca^{2+} flux to mitochondria suppressing cell transformation. Nature 54 549–553. https://doi.org/10.1038/nature22798.

[41] Ballirano, P., Cametti, G., 2015. Minerals in the human body. Crystal chemical and structural modifications of erionite fibers leached with simulated lung fluids. Am Miner 100, 103–112. https://doi.org/10.2138/am.2015.4922.

[42] Pacella, A., Ballirano, P., Fantauzzi, M., Rossi, A., Viti, C., Arrizza, L., Nardi, E., Caprioli, R., Montereali, M.R., 2021. Surface and bulk modifications of fibrous erionite in mimicked Gamble's solution at acidic pH. Minerals 11, 914. https://doi.org/10.3390/min11090914.

[43] Di Carlo, M.C., Ballirano, P., Montereali, M.R., Caprioli, R., Nardi, E., Pacella, A., 2023. An insight on possible toxicity mechanism of fibrous erionite. Period Min 92, 191–201. https://doi.org/10.13133/2239-1002/18097.

[44] Pacella, A., Cremisini, C., Nardi, E., Montereali, M.R., Pettiti, I., Ballirano, P., 2017. The mechanism of iron binding processes in erionite fibres. Sci Rep 7, 1319. https://doi.org/10.1038/s41598-017-01477-x.

[45] Pacella, A., Cremisini, C., Nardi, E., Montereali, M.R., Pettiti, I., Giordani, M., Mattioli, M., Ballirano, P., 2018. Different erionite species bind iron into the structure: a potential explanation for fibrous erionite toxicity. Minerals 8, 36. https://doi.org/10.3390/min8020036.

[46] Cannon, G.J., Swanson, J.A., 1992. The macrophage capacity for phagocytosis. J Cell Sci 101, 907–913. https://doi.org/10.1242/jcs.101.4.907.

[47] Raneri, S., Gianoncelli, A., Bonanni, V., Mirata, S., Scarfì, S., Fornasini, L., Bersani, D., Baroni, D., Picco, C., Gualtieri, A.F., 2024. The influence of cation exchange on the possible mechanism of erionite toxicity: a synchrotron-based micro-X-ray fluorescence study on THP-1-derived macrophages exposed to erionite-Na. Environ Res 252, 118878. https://doi.org/10.1016/j.envres.2024.118878.

[48] Hussell, T., Bell, T.J., 2014. Alveolar macrophages: Plasticity in a tissue-specific context. Nat Rev Immunol 14, 81–93. https://doi.org/10.1038/nri3600.

[49] Bassi, A.M., Mirata, S., Almonti, V., Tirendi, S., Vernazza, S., Fornasini, L., Raneri, S., Bersani, D., Passalacqua, M., Gualtieri, A.F., Scarfì, S., 2023. Cytotoxic and pro-inflammatory early effects of mineral fibres on human alveolar epithelial and immune cells. Period Miner 92, 223–239. https://doi.org/10.13133/2239-1002/18082.
[50] Di Giuseppe, D., Scarfì, S., Alessandrini, A., Bassi, A.M., Mirata, S., Almonti, V., Ragazzini, G., Mescola, A., Filaferro, M., Avallone, R., Vitale, G., Scognamiglio, V., Gualtieri, A.F., 2022. Acute cytotoxicity of mineral fibres observed by time-lapse video microscopy. Toxicology 466, 153081. https://doi.org/10.1016/j.tox.2021.153081.
[51] Mirata, S., Almonti, V., Di Giuseppe, D., Fornasini, L., Raneri, S., Vernazza, S., Bersani, D., Gualtieri, A.F., Bassi, A.M., Scarfì, S., 2022. The acute toxicity of mineral fibres: a systematic in vitro study using different THP-1 macrophage phenotypes. Int J Mol Sci 23, 2840. https://doi.org/10.3390/ijms23052840.
[52] Luzio, J.P., Pryor, P.R., Bright, N.A., 2007. Lysosomes: fusion and function. Nat Rev Mol Cell Bio 8, 622–632. https://doi.org/10.1038/nrm2217.
[53] Marques, M.R.C., Loebenberg, R., Almukainzi, M., 2011. Simulated biological fluids with possible application in dissolution testing. Dissolut Technol 18, 15–28. https://doi.org/10.14227/DT180311P15.
[54] Passaglia, E., 1970. The crystal chemistry of chabazites. Am Miner 55, 1278–1301.
[55] Bruker A.X.S., 2016. Topas V6: General profile and structure analysis software for powder diffraction data. Bruker AXS, Karlsruhe, Germany.
[56] Cheary, R.W., Coelho, A., 1992. Fundamental parameters approach to x-ray line-profile fitting. J Appl Crystallogr 25, 109–121. https://doi.org/10.1107/S0021889891010804.
[57] Passaglia, E., Ferro, O., 2002. Occurrence and crystal structure of magnesian chabazite. Stud Surf Sci Catal 142, 1729–1735. https://doi.org/10.1016/S0167-2991(02)80346-9.
[58] Le Page, Y., Donnay, G., 1976. Refinement of the crystal structure of low-quartz. Acta Crystallogr B 32, 2456–2459. https://doi.org/10.1107/S0567740876007966.
[59] Mattioli, M., Giordani, M., Ballirano, P., Salvioli Mariani, E., Bernardini, S., Della Ventura, G., 2023. First occurrence and characterization of erionite, a carcinogenic fibrous zeolite, from the volcanic rocks of Latium (Italy). Period Miner 92, 159–178. https://doi.org/10.13133/2239-1002/18084.
[60] Järvinen, M., 1993. Application of symmetrized harmonics expansion to correction of the preferred orientation effect. J Appl Crystallogr 26, 525–531. https://doi.org/10.1107/S0021889893001219.
[61] Sabine, T.M., Hunter, B.A., Sabine, W.R., Ball, C.J., 1998. Analytical expressions for the transmission factor and peak shift in absorbing cylindrical specimens. J Appl Crystallogr 31, 47–51. https://doi.org/10.1107/S0021889897006961.
[62] Ballirano, P., Maras, A., 2006. Mineralogical characterization of the blue pigment of Michelangelo's fresco "The Last Judgment. Am Miner 91, 997–1005. https://doi.org/10.2138/am.2006.2117.
[63] Ballirano, P., 2003. Effects of the choice of different ionization level for scattering curves and correction for small preferred orientation in Rietveld refinement: the $MgAl_2O_4$ test case. J Appl Crystallogr 36, 1056–1061. https://doi.org/10.1107/S0021889803010410.
[64] Chen, G., Yang, Y., Xu, C., Gao, S., 2018. A Flow cytometry-based assay for measuring mitochondrial membrane potential in cardiac myocytes after hypoxia/reoxygenation. J Vis Exp 137, 57725. https://doi.org/10.3791/57725.
[65] Stephenson, M.J., Attfield, M., Holmes, S.M., Dryfe, R.A.W., 2015. Electrochemically controlled ion exchange: proton ion exchange with sodium zeolite X and A. J Solid State Electr 19, 1985–1992. https://doi.org/10.1007/s10008-015-2851-6.
[66] Jones, J.B., 1968. Al-O and Si-O tetrahedral distances in aluminosilicate framework structures. Acta Crystallogr B 24, 355–358. https://doi.org/10.1107/S0567740868002360.
[67] Zhu, L., Seff, K., Olson, D.H., Cohen, B.J., Von Dreele, R.B., 1999. Hydronium Ions in Zeolites. I. Structures of Partially and Fully Dehydrated Na,H_3O-X by X-ray and Neutron Diffraction. J Phys Chem B 103, 10365–10372. https://doi.org/10.1021/jp991070z.
[68] Breck, D.W., Eversole, W.G., Milton, R.M., Reed, T.B., Thomas, T.L., 1956. Crystalline Zeolites. I. The properties of a new synthetic zeolite, Type A. J Am Chem Soc 78, 5963–5971. https://doi.org/10.1021/ja01604a001.
[69] Pérez-Botella, E., Valencia, S., Rey, F., 2022. Zeolites in adsorption processes: state of the art and future prospects. Chem Rev 122, 17647–17695. https://doi.org/10.1021/acs.chemrev.2c00140.
[70] Grifoni, E., Piccini, G.M., Lercher, J.A., Glezakou, V.-A., Rousseau, R., Parrinello, M., 2021. Confinement effects and acid strength in zeolites. Nat Commun 12, 2630. https://doi.org/10.1038/s41467-021-22936-0.
[71] Eckstein, S., Hintermeier, P.H., Zhao, R., Baráth, E., Shi, H., Liu, Y., Lercher, J.A., 2019. Influence of hydronium ions in zeolites on sorption. Angew Chem Int Ed 58, 3450–3455. https://doi.org/10.1002/anie.201812184.
[72] Farrugia, L.J., 1997. ORTEP-3 for Windows. University of Glasgow, Scotland.
[73] Giacobbe, C., Moliterni, A., Di Giuseppe, D., Malferrari, D., Wright, J.P., Mattioli, M., Ranieri, S., Giannini, C., Fornasini, L., Mugnaioli, E., Ballirano, P., Gualtieri, A.F., 2023. The crystal structure of the killer fibre erionite from Tuzköy (Cappadocia, Turkey). IUCrJ 10, 397–410. https://doi.org/10.1107/S2052252523003500.
[74] Niikura, K., 2006. Vacuolar ATPase as a drug discovery target. Drug N Perspect 19, 139–144. https://doi.org/10.1358/dnp.2006.19.3.977442.
[75] Yamashita, K., Nagai, H., Kondo, Y., Misawa, N., Toyokuni, S., 2013. Evaluation of two distinct methods to quantify the uptake of crocidolite fibers by mesothelial cells. J Clin Biochem Nutr 53, 27–35. https://doi.org/10.3164/jcbn.12-104.
[76] Alfonso, H., Franklin, P., Ching, S., Croft, K., Burcham, P., Olsen, N., Reid, A., Joyce, D., de Klerk, N., Musk, A.B., 2015. Effect of N-acetylcysteine supplementation on oxidative stress status and alveolar inflammation in people exposed to asbestos: a double-blind, randomized clinical trial. Respirology 20, 1102–1107. https://doi.org/10.1111/resp.12592.
[77] Fiorilla, I., Martinotti, S., Todesco, A.M., Bonsignore, G., Cavaletto, M., Patrone, M., Ranzato, E., Audrito, V., 2023 Aug 11. Chronic inflammation, oxidative stress and metabolic plasticity: three players driving the pro-tumorigenic microenvironment in malignant mesothelioma. Cells 12 (16), 2048. https://doi.org/10.3390/cells12162048.
[78 Dumortier, P., De Maertelaer, V., 2001. Erionite bodies and fibres in bronchoalveolar lavage fluid (BALF) of residents from Tuzköy, Cappadocia, Turkey. Occup Environ Med 58, 261–266. https://doi.org/10.1136/oem.58.4.261.
[79] Xiong, J., Zhu, M.X., 2016. Regulation of lysosomal ion homeostasis by channels and transporters. Sci China Life Sci 59, 777–791. https://doi.org/10.1007/s11427-016-5090-x.
[80] Ruiz-Agudo, E., Putnis, C.V., Rodriguez-Navarro, C., Putnis, A., 2011. Effect of pH on calcite growth at constant aCa^{2+}/aCO_3^{2-} ratio and supersaturation. Geochim Cosmochim Acta 75, 284–296. https://doi.org/10.1016/j.gca.2010.09.034.
[81] Pasteris, J.D., Wopenka, B., Valsami-Jones, E., 2008. Bone and tooth mineralization: why apatite. Elements 4, 97–104. https://doi.org/10.2113/GSELEMENTS.4.2.97.
[82] Wood, S.A., Taunton, A.E., Normand, C., Gunter, M.E., 2006. Mineral-fluid interactions in the lungs: insights from reaction path modeling. Inhal Toxicol 18, 975–984. https://doi.org/10.1080/08958370600835252.